J. Fluid Mech. (1999), *vol.* 379, *pp.* 105–143. Printed in the United Kingdom

A numerical study of the modulation of isotropic turbulence by suspended particles

By SHIVSHANKAR SUNDARAM† AND LANCE R. COLLINS‡

Department of Chemical Engineering, The Pennsylvania State University, University Park, PA 16802, USA

(Received 2 March 1997 and in revised form 21 July 1998)

Direct numerical simulations of a turbulent fluid laden with finite-sized particles are performed. The computations, on a 128^3 grid along with a maximum of 262 144 particles, incorporated both direct particle interactions via hard-sphere collisions and particle feedback. The 'reverse' coupling is accomplished in a manner ensuring correct discrete energy conservation (Sundaram & Collins 1996). A novel two-field formalism (Sundaram & Collins 1994*a*) is employed to calculate two-point correlations and equivalent spectral densities. An important consideration in these simulations is the initial state of fluid and particles. That is, the initial conditions must be chosen so as to allow a meaningful comparison of the different runs. Using such a carefully initialized set of runs, particle inertia was observed to increase both the viscous and drag dissipations; however, simultaneously, it also caused particle velocities to correlate for longer distances. The combination of effects suggests a mechanism for turbulence enhancement or suppression that depends on the parameter values. Like previous investigators, 'pivoting' or crossover of the fluid energy spectra was observed. A possible new scaling for this phenomenon is suggested. Furthermore, investigations of the influence of particle mass and number densities on turbulence modulation are also carried out.

1. Introduction

A fundamental understanding of the nature of turbulent solid–fluid flows is of importance in many atmospheric (e.g. pollutant transport and raindrop growth), industrial (e.g. aerosol processing and solids transport) and even physiological processes (e.g. arterial/pulmonary transport). Problems targeted for investigation in particulate flows usually involve particle dispersion, turbulence modulation or particle coagulation. Separate studies focusing on a selected problem are required as dispersion is essentially controlled by large-scale motion of fluid turbulence in contrast with turbulence modulation and coagulation which are thought to be primarily driven by small scales. This study deals exclusively with aspects of turbulence modification by suspended, heavy particles.

There are three distinct regimes in particle–fluid flows characterized by the particle volume and mass concentrations. First, at very low volume and mass loadings, the particles do not affect the surrounding flow and are themselves only transported by the local flow – termed 'one-way' coupling. The unmodified turbulence is solved using well

† Present address: CFD Research Corporation, 2 Lakeview Ave., Piscataway NJ 08854, USA.
‡ Author to whom correspondence should be addressed.

understood single-phase models. The passive advection of particles can be adequately characterized using stochastic (see reviews by Crowe, Troutt & Chung 1996 or Shirolkar, Coimbra & McQuay 1996) or deterministic (see reviews by McLaughlin 1994 or Elghobashi 1991 or the older description of modelling approaches by Crowe 1982) models of choice. The second regime includes suspensions that are low in volumetric concentrations due to small particle sizes, yet have moderately high mass loadings, attributable to high particle densities. Conventional wisdom dictates that particle–particle interactions, both direct (collisions) and hydrodynamic can be neglected in this regime. However, new findings on the particle-concentration fields, which will be discussed later in this paper, suggest that direct particle interactions may still play an important role. Furthermore, even though the volume fraction of particles is small, the solid particles significantly alter the nature of the continuous-phase turbulence – hence 'two-way' or 'reverse' coupling must be taken into consideration. Thirdly, at high particle volume concentrations (and mass concentrations) particle dynamics become collision-dominated and the fluid mechanics under low void fraction conditions becomes nearly intractable. This regime is sometimes referred to as 'granular flow'. In this study we will be primarily addressing particulate suspensions that are in the volumetrically dilute, though appreciably mass loaded (or second) regime.

There is a large body of experimental work on dilute, particulate turbulence in jet, pipe and channel flow configurations (Tsuji 1991). Under a particle load, some investigators reported augmentation of the fluid-phase turbulence while others observed the contrary. Gore & Crowe (1989) attempted to correlate the above behaviour in terms of a single length scale parameter σ/l_e, where σ is the particle diameter and l_e is the integral length scale of the turbulence. A serious drawback in this reasoning was the non-inclusion of particle density which, along with size, determines particle inertia. The ability of particles to respond to the multiple scales of turbulent motion is considered the primary factor in determining turbulence modification. Hetsroni (1989) included particle inertia in his analysis and suggested that a cutoff for turbulence augmentation or suppression be based on the particle Reynolds number, Re_p. Yuan & Michaelides (1994) obtained a simple expression for turbulence modulation involving particle parameters and turbulence intensity, based on a balance between turbulence reduction caused by the work required to accelerate the particles and turbulence production due to particle wakes. Yarin & Hetsroni (1994) proposed another model based on a combination of mixing length and kinetic energy balance methods. While they show fair agreement with the data, both theories do involve ad hoc modelling procedures leaving many questions regarding turbulence modulation still unanswered.

Spectral methods, in combination with modern day computers, provide the means to simulate turbulence with very high accuracy, free from any ad hoc modelling. The bulk of numerical simulation studies on particle-laden turbulent flows have focused on particle-phase phenomena such as dispersion and settling. More recent work has focused on the energy exchange between the phases by incorporating the particle forces into the fluid equation of motion (so called reverse coupling). For example, Pan & Bannerjee (1997) simulated the motion of large heavy particles entrained in a turbulent channel flow. They showed that the particles influence the ejection–sweep processes responsible for generating Reynolds stress near the wall, thereby enhancing or diminishing the turbulence depending on particle size. The results are relevant to the present study; however, their simulation was limited to particles much larger than the Kolmogorov scale, whereas the present study focuses on particles that are smaller than the Komogorov scale. Nevertheless, the general trends they observe are consistent with our observations.

Two prior investigators have simulated modulation of turbulence by small particles in a homogeneous, isotropic setting. Squires & Eaton (1990) studied point-sized particles in turbulence subject to Stokes drag. As external forcing was used in their simulation to produce stationary turbulence, it is not possible to draw general conclusions from their study regarding the partitioning of energy between particles and fluid. However, they did report that the particles augmented the energy content of the fluid at high wavenumbers while decreasing it at low wavenumbers with the net effect, apparently dissipative. This result, while intuitively reasonable, needed further verification as forcing schemes do affect spectral dynamics in the low wavenumber region. Elghobashi & Truesdell (1993) carried out a similar study, but in decaying turbulence both with and without gravitational forces. It was found that particles, in the absence of gravity, consistently decreased levels of fluid turbulence. With gravity included, they found that the particles could increase fluid turbulence. They also observed a similar 'pivoting' or 'crossover' of the laden fluid spectrum when compared with that of the unladen flow. Transfer spectra exhibited identical behaviour and it was concluded that particles modulate turbulence by altering the inertial transfer mechanism. Unfortunately, their study cannot precisely identify the mechanism responsible for the pivot in the fluid energy spectrum because the pivot results from a change in the energy transfer mechanism (as they suggest) and from energy exchange between the two phases. Considering the fluid phase alone cannot distinguish between these mechanisms. The present spectral analysis takes into consideration both the fluid and particle phases and thus allows us to pinpoint the origin of the pivot in the energy spectrum.

Other DNS calculations by Squires & Eaton (1991) and Wang & Maxey (1993) showed, using forced turbulence, that the particle concentration field is non-uniform and that particles preferentially accumulate in low-vorticity regions of the flow. Sundaram & Collins (1997) observed a persistence of this phenomenon even in the presence of particle interactions in the form of hard-sphere collisions, which counteract the inertial effect responsible for segregating the particles. This result is important because it indicates that even uniformly distributed particle systems will eventually segregate into particle-rich and particle-lean subregions, depending on the size and mass of the particles. Moreover, due to high local concentrations, turbulence modulation may be significant even at low mean concentrations.

A complementary approach to simulation of particle-laden flows is to use models that describe average properties of the two-phase flow field. The most prevalent approach to modelling multiphase, and specifically, particulate flows is based upon a two-fluid approach, wherein both the fluid and particle phases are treated as interpenetrating continua. Following the formulation of the continuity and momentum equations for each phase, unknown terms are either closed directly or additional equations are generated. Closures are then postulated for the new equations, along with the introduction of a new class of empirical constants prescribing the interaction or exchange between the two phases. Empirical constants with analogues to single-phase formulations are rarely altered from their single-phase equivalents, while new constants are fixed by comparing the model predictions to experimental measurements. Such models of the k–ϵ family, with additionally generated transport equations, have met with only limited success (Ishii 1975; Elghobashi & Abou-Arab 1983; Besnard & Harlow 1985).

Implicit in all simple two-equation models of turbulence, such as the k–ϵ model, is the assumption that the energy spectrum rapidly relaxes into a universal shape that is completely characterized by the two turbulence properties. This characteristic of turbulence has been observed and is widely accepted in single-phase turbulence, even in complex geometries. However, the existence of an universal energy spectrum for

particle-laden turbulent flows has yet to be established. For example, the particle size and response time introduce new scales into the dynamics of the energy spectrum which may potentially disrupt the attainment of spectral self-similarity. Thus, the foundation for the simple models of particle-laden turbulent flows is lacking.

It is our belief that the statistical properties of the total two-phase system, only, provide a basis for understanding the coupling of the two phases. The absence of work on the total energy spectrum is due in part to the lack of a methodology to compute spectral statistics equivalent to single-phase flows. In previous research, Sundaram & Collins (1994*a,b*) developed such a formalism by treating the particle–fluid system as a single 'pseudo-fluid' with density variations occurring discontinuously at particle interfaces. Because all points in the system, within both the fluid and particle phases, are well defined and equivalent, definitions for two-point correlations remain the same as in incompressible turbulence. The only minor complication is that in the particulate system, correlations involving fluid–fluid, fluid–particle, and particle–particle must be accounted for separately; however, this only increases the bookkeeping but otherwise poses no fundamental change from the single-phase case.

The first two-point statistic that will be discussed is the density correlation, defined as $\overline{\rho'(\boldsymbol{x})\rho'(\boldsymbol{x}+\boldsymbol{r})}$, where ρ' denotes the fluctuation about the mean density and the overbar implies an ensemble average. Aside from being the simplest of the two-point statistics, the density correlation is also known to play a significant dynamic role in the evolution of particle-laden flows. For example, in the presence of a mean pressure gradient, the density correlation is known to create an important source of turbulent energy in multiphase flows (Clark & Spitz 1994). Consequently, much attention has been devoted to correlations of the density field in various modelling efforts (Besnard & Harlow 1985; Clark & Spitz 1994; Besnard *et al.* 1990).

The advantages of using multi-point statistics to analyse a particle-laden system can be illustrated in the following manner. Consider two identical volumes of fluid, each containing N_p particles of the same density and diameter. The first system (I) contains particles that are randomly distributed throughout the volume while the second system (II) has regions of high and low particle concentration (note, this is a realistic scenario since particles do accumulate in regions of low vorticity, as will be shown). If we consider the entire volume as a whole, the single-point mean density autocorrelation can be shown to be $\overline{\rho'^2} = \alpha_p\alpha_f(\rho_p - \rho_f)^2$, where α_p and α_f are the volume fractions of particles and fluid respectively, and ρ_p and ρ_f are the particle and fluid densities respectively. As the particle and fluid volume fractions are functions of N_p only, the single-point density correlations for the two systems are identical. However, the dynamic response of these two systems to a gravitational field or a pressure gradient will be quite different, and so any reasonable description of these systems must incorporate the spatial distribution of the particles.

Besnard & Harlow (1985) attempted to accomplish this by allowing the volume fractions themselves to 'fluctuate' to represent the high and low concentrations of the particles in the system. Unfortunately, this introduces an ambiguity into the model because the magnitude of the fluctuations of the volume fractions will depend on the size of the volume over which averages are computed, which is completely arbitrary. The alternative approach taken here uses the two-point density correlation to characterize the system. This statistic is inherently superior because it accounts for the particle distribution as a continuous function of the separation distance; thus, it does not introduce an artificial volume size into its averaging procedure. Moreover, the two-point density correlation (or spectrum) has the flexibility to separate out the influence of all of the different length scales in the system. We believe this is crucial

for capturing the complex interaction between the two phases at the different scales of motion.

In this study, we extend the earlier work to compute the Reynolds stress and energy spectrum. Critical *intra* and *inter* phase correlations are identified and determined from direct numerical simulations of decaying isotropic turbulence performed on a 128^3 grid. Because we consider the total energy, the complex mechanisms responsible for energy exchange between the two phases are not relevant, and instead the focus is on the mechanisms that either enhance or diminish the total kinetic energy in the system. Our results show that in the absence of source terms (e.g. due to mean flow gradients, gravity, etc.), particles manifestly reduce the turbulent kinetic energy by increasing the viscous dissipation rate.

This raises an important question. If particles are manifestly dissipative, how then can they ever enhance the turbulent kinetic energy of a flow? The only satisfactory explanation appears to be that particles must, by some unknown mechanism, augment the production rate of turbulence as well. Unfortunately, the simulations performed in this study do not contain a turbulence source term so we cannot determine the mechanism responsible for enhancing the production rate. Nevertheless, our results do suggest a possible new mechanism by which particles may enhance the mean shear (i.e. vortex stretching) production rate. The details of the proposed mechanism are presented in §7.

The paper is organized as follows: §2 outlines the essential details of the spectral analysis of particulate flows, and §3 discusses simplifications of the theory for the conditions of this study. The governing equations for the numerical simulations as well as the numerical methods used are set out in §4. Single-point energies and dissipations from the simulations are discussed in §5. Next, two-point correlations and spectra are presented beginning with the density correlation in §6, followed by the velocity correlations and spectra in §7. The results are summarized in §8.

2. Theory

The methodology developed earlier to compute two-point correlations in particulate flows (Sundaram & Collins 1994*a*) will be briefly reviewed here. We consider a canonical ensemble of systems, each having a total volume V embedded with precisely N_p non-deformable, spherical particles each of diameter σ and density ρ_p, dispersed in a fluid of density ρ_f. Note that for a periodic system the volume V is assumed to be an integer multiple of the natural period of the system. We then define the centre of the nth particle to be $\boldsymbol{x}^n$ and its velocity to be $\boldsymbol{v}^n$. All two-point correlations in such a system can be expressed as a sum of contributions over the particle phase alone, fluid phase alone and between particle and fluid phases. This breakup, while increasing the number of unknowns to be tracked, is necessary to describe two-point correlations in a two-phase system. We start by defining an identifier (or colour) function to distinguish the particle phase from the fluid phase:

$$\beta_p(\boldsymbol{x}) = \begin{cases} 1 & \text{within particle phase} \\ 0 & \text{otherwise,} \end{cases} \tag{1}$$

$$\beta_f(\boldsymbol{x}) = 1 - \beta_p(\boldsymbol{x}). \tag{2}$$

Hereafter, indices p and f will be used solely to denote the particulate and fluid phases respectively. Mathematically, the particle colour function can be written in the

following manner:

$$\beta_p(\boldsymbol{x}) = \sum_{n=1}^{N_p} H\left(\frac{\sigma}{2} - |\boldsymbol{x} - \boldsymbol{x}^n|\right), \tag{3}$$

where H represents the Heaviside (or unit step) function. By definition, the ensemble averages of the colour functions are

$$\overline{\beta_p(\boldsymbol{x})} = \alpha_p, \tag{4}$$

$$\overline{\beta_f(\boldsymbol{x})} = \alpha_f, \tag{5}$$

where α_p and α_f are the particle and fluid volume fractions, respectively. In addition, a fluctuating component of the colour functions may be defined as

$$\beta_p'(\boldsymbol{x}) = \beta_p(\boldsymbol{x}) - \alpha_p = \sum_{n=1}^{N_p} H\left(\frac{\sigma}{2} - |\boldsymbol{x} - \boldsymbol{x}^n|\right) - \alpha_p, \tag{6}$$

$$\beta_f' = -\beta_p'. \tag{7}$$

If we now consider an arbitrary function $\Gamma(\boldsymbol{x})$ (say), which is continuous in either phase but is allowed to change discontinuously at the phase boundaries (i.e. particle interfaces), the 'phase' averages can be defined as

$$\overline{\Gamma}^p \equiv \frac{\overline{\beta_p(\boldsymbol{x})\Gamma(\boldsymbol{x})}}{\alpha_p}, \tag{8}$$

$$\overline{\Gamma}^f \equiv \frac{\overline{\beta_f(\boldsymbol{x})\Gamma(\boldsymbol{x})}}{\alpha_f}, \tag{9}$$

where the superscripts indicate averaging within that phase only. It then follows that the ensemble average of Γ can be written as

$$\overline{\Gamma} = \alpha_p \overline{\Gamma}^p + \alpha_f \overline{\Gamma}^f \tag{10}$$

and the overall fluctuation, defined as $\Gamma'(\boldsymbol{x}) \equiv \Gamma(\boldsymbol{x}) - \overline{\Gamma}$, by

$$\Gamma'(\boldsymbol{x}) = (\overline{\Gamma}^p - \overline{\Gamma}^f)\beta_p'(\boldsymbol{x}) + \Gamma_p'(\boldsymbol{x}) + \Gamma_f'(\boldsymbol{x}), \tag{11}$$

where $\Gamma_p'(\boldsymbol{x}) \equiv \beta_p(\boldsymbol{x})(\Gamma(\boldsymbol{x}) - \overline{\Gamma}^p)$ and $\Gamma_f'(\boldsymbol{x}) \equiv \beta_f(\boldsymbol{x})(\Gamma(\boldsymbol{x}) - \overline{\Gamma}^f)$ represent the 'phase' fluctuations. The accompanying colour functions serve as a reminder that these phase fluctuations are defined within the respective phases only. Equation (11) states that overall fluctuations may be caused by differences in the mean value in the two phases and by variations of the quantity within each of the phases (phase fluctuations). A generic two-point correlation is then given by

$$\begin{aligned}
\overline{\Gamma'(\boldsymbol{x})\Gamma'(\boldsymbol{x}+\boldsymbol{r})} = {} & \underbrace{(\overline{\Gamma}^p - \overline{\Gamma}^f)^2\, \overline{\beta_p'(\boldsymbol{x})\beta_p'(\boldsymbol{x}+\boldsymbol{r})}}_{\text{distributional}} \\
& + \underbrace{\overline{\beta_p(\boldsymbol{x})\Gamma_p'(\boldsymbol{x})\beta_p(\boldsymbol{x}+\boldsymbol{r})\Gamma_p'(\boldsymbol{x}+\boldsymbol{r})}}_{\text{particle-particle}} + \underbrace{\overline{\beta_f(\boldsymbol{x})\Gamma_f'(\boldsymbol{x})\beta_f(\boldsymbol{x}+\boldsymbol{r})\Gamma_f'(\boldsymbol{x}+\boldsymbol{r})}}_{\text{fluid-fluid}} \\
& + \underbrace{\overline{\beta_f(\boldsymbol{x})\Gamma_f'(\boldsymbol{x})\beta_p(\boldsymbol{x}+\boldsymbol{r})\Gamma_p'(\boldsymbol{x}+\boldsymbol{r})} + \overline{\beta_p(\boldsymbol{x})\Gamma_p'(\boldsymbol{x})\beta_f(\boldsymbol{x}+\boldsymbol{r})\Gamma_f'(\boldsymbol{x}+\boldsymbol{r})}}_{\text{fluid-particle}} \\
& + \underbrace{\Big[\, \overline{\beta_p(\boldsymbol{x})\beta_p(\boldsymbol{x}+\boldsymbol{r})\Gamma_p'(\boldsymbol{x}+\boldsymbol{r})} + \overline{\beta_p(\boldsymbol{x}+\boldsymbol{r})\beta_p(\boldsymbol{x})\Gamma_p'(\boldsymbol{x})} \\
& + \overline{\beta_p(\boldsymbol{x})\beta_f(\boldsymbol{x}+\boldsymbol{r})\Gamma_f'(\boldsymbol{x}+\boldsymbol{r})} + \overline{\beta_p(\boldsymbol{x}+\boldsymbol{r})\beta_f(\boldsymbol{x})\Gamma_f'(\boldsymbol{x})} \,\Big] \left(\overline{\Gamma}^p - \overline{\Gamma}^f\right)}_{\text{cross terms}}.
\end{aligned} \tag{12}$$

For a given two-point correlation, relationships are derived for each of the component correlations shown in (12), and the complete correlation is then obtained by summing.

2.1. *Density correlation*

We begin with the simplest two-point correlation that can be defined, the density correlation, defined as

$$B(\boldsymbol{r}) = \overline{\rho'(\boldsymbol{x})\rho'(\boldsymbol{x}+\boldsymbol{r})}. \tag{13}$$

Using the previously defined identifier functions the overall density can be expressed as

$$\rho'(\boldsymbol{x}) = \beta_p'(\boldsymbol{x})(\rho_p - \rho_f). \tag{14}$$

Note that since the density within each phase is constant, the other terms in (11) are identically zero. Substituting the above expression for the density fluctuation yields

$$B(\boldsymbol{r}) = \overline{\beta_p'(\boldsymbol{x})\beta_p'(\boldsymbol{x}+\boldsymbol{r})}(\rho_p - \rho_f)^2. \tag{15}$$

The correlation $\overline{\beta_p'(\boldsymbol{x})\beta_p'(\boldsymbol{x}+\boldsymbol{r})}$ is a function of the configurational arrangement of the particles. In earlier work (Sundaram & Collins 1994*a*), we derived an exact relationship between the β-correlation and the particle radial distribution function, $\tilde{g}^{pp}(\boldsymbol{r})$. The resulting expression for the density correlation was

$$B(\boldsymbol{r}) = \left[\frac{\alpha_p}{V_p} I(r) + \left(\frac{\alpha_p}{V_p}\right)^2 \int_V \tilde{h}^{pp}(|\boldsymbol{z}|) I(|\boldsymbol{r}-\boldsymbol{z}|)\, \mathrm{d}\boldsymbol{z}\right](\rho_p - \rho_f)^2, \tag{16}$$

where

$$\tilde{h}^{pp}(\boldsymbol{z}) = \tilde{g}^{pp}(\boldsymbol{z}) - 1, \tag{17}$$

$$I(r) = \begin{cases} V_p[1 - \frac{3}{2}r/\sigma + \frac{1}{2}(r/\sigma)^3], & r/\sigma \leqslant 1 \\ 0, & r/\sigma > 1, \end{cases} \tag{18}$$

and V_p is the volume of the particle (i.e. $\pi\sigma^3/6$). The function $I(r)$ is referred to as the 'overlap function' because it is defined as the volume of overlap between two spheres separated by a distance $r \equiv |\boldsymbol{r}|$. Note that $\tilde{}$ is used throughout to distinguish particle centre statistics from those averaged over the particle phase, and the superscript '*pp*' identifies a particle–particle correlation.

The above relationship (16) can be understood as follows. The first term within the square brackets represents the contribution arising from intra-particle correlations, whereas the second term accounts for the inter-particle correlations. The inter-particle correlation is a function of the location of particle centres, which in turn is described by the particle radial distribution function (RDF), $\tilde{g}^{pp}(\boldsymbol{r})$ (or more precisely, $\tilde{h}^{pp}(\boldsymbol{r}) = \tilde{g}^{pp}(\boldsymbol{r}) - 1$). The definition of the RDF itself can be simply stated as the normalized expectancy of finding a second particle at a distance $\boldsymbol{r}$ from any given particle. For a homogeneous system this may be stated as (McQuarrie 1976)

$$\tilde{g}^{pp}(\boldsymbol{r}) = \frac{N_p(N_p-1)}{n^2} \int_V \cdots \int_V P^{(N_p)}(\boldsymbol{x}^1, \cdots, \boldsymbol{x}^{N_p})\, \mathrm{d}\boldsymbol{x}^3 \cdots \mathrm{d}\boldsymbol{x}^{N_p}, \tag{19}$$

where $\boldsymbol{r} \equiv \boldsymbol{x}^1 - \boldsymbol{x}^2$, $n = N_p/V$ is the number density of particles and $P^{(N_p)}\mathrm{d}\boldsymbol{x}^1 \cdots \mathrm{d}\boldsymbol{x}^{(N_p)}$ represents the probability of finding particle 1 distributed within a volume $\mathrm{d}\boldsymbol{x}^1$ centred at point $\boldsymbol{x}^1$, and so on; note that the probability is normalized such that

$$\int_V \cdots \int_V P^{(N_p)}(\boldsymbol{x}^1, \cdots, \boldsymbol{x}^{N_p})\, \mathrm{d}\boldsymbol{x}^1 \cdots \mathrm{d}\boldsymbol{x}^{N_p} = 1. \tag{20}$$

There are two important properties of $B(\boldsymbol{r})$ that are worth noting. First, its value at $\boldsymbol{r} = 0$ (i.e. single-point value) is related to the volume fraction of the particles by

$$B(0) = \overline{\rho^2} - \bar{\rho}^2 = \alpha_p \alpha_f (\rho_p - \rho_f)^2. \tag{21}$$

Secondly, its integral over the system volume V vanishes (Sundaram & Collins 1994*a*)

$$\int_V B(\boldsymbol{r})\, \mathrm{d}\boldsymbol{r} = 0. \tag{22}$$

Given this boundedness, it is possible to define the Fourier transform of (16) and thereby obtain the density correlation spectrum. Omitting the details (Sundaram & Collins 1994*a*), the final result is

$$\hat{B}(\boldsymbol{k}) = \frac{\alpha_p}{V_p} \hat{I}(k) \left[1 + \frac{\alpha_p}{V_p} \hat{\tilde{h}}^{pp}(\boldsymbol{k}) \right] (\rho_p - \rho_f)^2, \tag{23}$$

where

$$\hat{I}(k) = 144 V_p^2 \frac{\Big(k\sigma \cos(k\sigma/2) - 2 \sin(k\sigma/2) \Big)^2}{(k\sigma)^6}. \tag{24}$$

In order to evaluate $B(\boldsymbol{r})$ and $\hat{B}(\boldsymbol{k})$, we will need to determine the radial distribution functions, or to be more precise $\tilde{h}^{pp}(\boldsymbol{r})$ and $\hat{\tilde{h}}^{pp}(\boldsymbol{k})$. In the earlier study (Sundaram & Collins 1994*a*), these particle field statistics were approximated by using the Percus–Yevick solution for hard-sphere gases (Percus & Yevick 1958). This approximation is valid for very high mass loadings (granular systems), but cannot be used in the present circumstance. Instead, they are determined from the direct numerical simulations. The details of the evaluation of these properties from the simulations are discussed separately in §6.

2.2. *Reynolds stress*

For a given particle–fluid system, the velocity fluctuation can be decomposed in the following manner:

$$u_i'(\boldsymbol{x}) = \beta_p(\boldsymbol{x}) v_i(\boldsymbol{x}) + \beta_f(\boldsymbol{x}) u_i^f(\boldsymbol{x}), \tag{25}$$

where $v_i(\boldsymbol{x})$ is a shorthand notation for the velocity of the particle that overlaps point $\boldsymbol{x}$, or more precisely $v_i(\boldsymbol{x}) \equiv \sum_{n=1}^{N_p} H\left(\frac{1}{2}\sigma - |\boldsymbol{x} - \boldsymbol{x}^n|\right) v_i^n$. Hereafter, the superscript f in $u_i^f(\boldsymbol{x})$ will be suppressed, and instead we adopt the convention that the variable u (without a prime) is reserved exclusively for fluid velocities while v is for particle velocities. Note that the velocity within either phase is not constant (as was the case with density), but the phase-averaged values vanish because there is zero net flow in this isotropic system. Hence, the distributional and cross terms in (12) vanish.

A generalized Reynolds stress tensor can be defined as

$$R_{ij}(\boldsymbol{x}, \boldsymbol{x} + \boldsymbol{r}) \equiv \overline{\rho(\boldsymbol{x}) u_i'(\boldsymbol{x}) u_j'(\boldsymbol{x} + \boldsymbol{r})}. \tag{26}$$

For homogeneous fields, $R_{ij}(\boldsymbol{x}, \boldsymbol{x} + \boldsymbol{r}) = R_{ij}(\boldsymbol{r})$. Substituting (25) into (26), we obtain

$$R_{ij}(\boldsymbol{r}) = R_{ij}^{ff}(\boldsymbol{r}) + R_{ij}^{fp}(\boldsymbol{r}) + R_{ij}^{pf}(\boldsymbol{r}) + R_{ij}^{pp}(\boldsymbol{r}), \tag{27}$$

where

$$R_{ij}^{ff}(\boldsymbol{r}) = \rho_f \quad \overline{\beta_f(\boldsymbol{x}) u_i(\boldsymbol{x})\, \beta_f(\boldsymbol{x} + \boldsymbol{r}) u_j(\boldsymbol{x} + \boldsymbol{r})}, \tag{28a}$$

$$R_{ij}^{fp}(\boldsymbol{r}) = \rho_f \quad \overline{\beta_f(\boldsymbol{x}) u_i(\boldsymbol{x})\, \beta_p(\boldsymbol{x} + \boldsymbol{r}) v_j(\boldsymbol{x} + \boldsymbol{r})}, \tag{28b}$$

$$R_{ij}^{pf}(\boldsymbol{r}) = \rho_p \quad \overline{\beta_p(\boldsymbol{x})v_i(\boldsymbol{x})\,\beta_f(\boldsymbol{x}+\boldsymbol{r})u_j(\boldsymbol{x}+\boldsymbol{r})}, \tag{28c}$$

$$R_{ij}^{pp}(\boldsymbol{r}) = \rho_p \quad \overline{\beta_p(\boldsymbol{x})v_i(\boldsymbol{x})\,\beta_p(\boldsymbol{x}+\boldsymbol{r})v_j(\boldsymbol{x}+\boldsymbol{r})}. \tag{28d}$$

R_{ij}^{ff},R_{ij}^{fp}, R_{ij}^{pf}, and R_{ij}^{pp} refer to fluid–fluid, fluid–particle, particle–fluid and particle–particle correlations respectively. The single-point values for these correlations can be shown to be

$$R_{ij}^{ff}(0) = \rho_f \alpha_f \overline{u_i u_j}^f, \tag{29a}$$

$$R_{ij}^{pp}(0) = \rho_p \alpha_p \overline{v_i v_j}^p, \tag{29b}$$

$$R_{ij}^{fp}(0) = R_{ij}^{pf}(0) = 0; \tag{29c,d}$$

hence,

$$R_{ij}(0) = \rho_p \alpha_p \overline{v_i v_j}^p + \rho_f \alpha_f \overline{u_i u_j}^f. \tag{29e}$$

Once again, the superscripts adjacent to the overbars indicate conditional averages within that field only. The cross terms (fluid–particle and particle–fluid) are identically zero because the particle phase excludes the fluid phase, following (1). The decomposition shown in (29*e*) forms the basis of numerous two-phase models in the literature; however, our intent here is to analyse the complete two-point correlation and not just the single-point moments.

As mentioned before, velocity correlations over each phase and across the phases have to be treated separately. First, we present expressions for each component of the Reynolds stress (see Appendix A for details):

$$R_{ij}^{ff}(\boldsymbol{r}) = \alpha_f^2 \rho_f \tilde{g}^{ff}(\boldsymbol{r}) \tilde{E}_{ij}^{ff}(\boldsymbol{r}), \tag{30}$$

$$R_{ij}^{fp}(\boldsymbol{r}) = \left(\frac{\alpha_p \alpha_f}{V_p}\right) \rho_f \int_V H\left(\frac{\sigma}{2} - |\boldsymbol{r}-\boldsymbol{z}|\right) \tilde{g}^{fp}(\boldsymbol{z}) \tilde{E}_{ij}^{fp}(\boldsymbol{z})\, \mathrm{d}\boldsymbol{z}, \tag{31}$$

$$R_{ij}^{pf}(\boldsymbol{r}) = \left(\frac{\alpha_p \alpha_f}{V_p}\right) \rho_p \int_V H\left(\frac{\sigma}{2} - |\boldsymbol{r}-\boldsymbol{z}|\right) \tilde{g}^{pf}(\boldsymbol{z}) \tilde{E}_{ij}^{pf}(\boldsymbol{z})\, \mathrm{d}\boldsymbol{z}, \tag{32}$$

$$R_{ij}^{pp}(\boldsymbol{r}) = \rho_p \frac{\overline{v_p^2}}{3} \frac{\alpha_p}{V_p} I(|\boldsymbol{r}|)\delta_{ij} + \left(\frac{\alpha_p}{V_p}\right)^2 \rho_p \int_V \tilde{g}^{pp}(|\boldsymbol{z}|) \tilde{E}_{ij}^{pp}(|\boldsymbol{z}|) I(|\boldsymbol{r}-\boldsymbol{z}|)\, \mathrm{d}\boldsymbol{z}. \tag{33}$$

$\tilde{E}_{ij}^{ff}$, $\tilde{E}_{ij}^{fp}$, $\tilde{E}_{ij}^{pf}$ and $\tilde{E}_{ij}^{pp}$ represent conditional correlations involving only the velocities at particle centres and/or fluid points:

$$\tilde{E}_{ij}^{ff}(\boldsymbol{r}) = \left[\overline{u_i(\boldsymbol{x})u_j(\boldsymbol{x}+\boldsymbol{r}) \mid \beta_f(\boldsymbol{x}) = 1; \beta_f(\boldsymbol{x}+\boldsymbol{r}) = 1}\right], \tag{34}$$

$$\tilde{E}_{ij}^{fp}(\boldsymbol{r}) = \left[\overline{u_i(\boldsymbol{x})v_j^m \mid \beta_f(\boldsymbol{x}) = 1; \boldsymbol{x}^m = \boldsymbol{x}+\boldsymbol{r}}\right], \tag{35}$$

$$\tilde{E}_{ij}^{pf}(\boldsymbol{r}) = \left[\overline{v_i^m u_j'(\boldsymbol{x}+\boldsymbol{r}) \mid \boldsymbol{x}^m = \boldsymbol{x}; \beta_f(\boldsymbol{x}+\boldsymbol{r}) = 1}\right], \tag{36}$$

$$\tilde{E}_{ij}^{pp}(\boldsymbol{r}) = \left[\overline{v_i^m v_j^n \mid \boldsymbol{x}^m = \boldsymbol{x}; \boldsymbol{x}^n = \boldsymbol{x}+\boldsymbol{r}}\right], \tag{37}$$

where here the overbars indicate conditional ensemble averages, and the conditions to be satisfied are shown to the right of the vertical line. At the risk of nomenclature

confusion, $\tilde{E}_{ij}$ – the density free velocity correlations involving particle centres – are introduced here to distinguish phase-averaged quantities (R_{ij}) from particle-centre quantities ($\tilde{E}_{ij}$). The particle-centre statistics are obtained directly from DNS and the phase-averaged quantities are computed from (30)–(33).

In (30)–(33) $\tilde{g}^{pp}$ refers to the classical particle–particle radial distribution function (19); $\tilde{g}^{ff}$, $\tilde{g}^{fp}$, and $\tilde{g}^{pf}$ are concise notations for the radial distribution functions associated with the fluid–fluid, fluid–particle, and particle–fluid correlations respectively. However, it must be noted that these distribution functions are not independent and are related to $\tilde{g}^{pp}$. These relations in physical and spectral space are listed in Appendix B.

The only assumption imposed thus far is homogeneity of the velocity field. The further assumptions of isotropy, dilute particle volume fractions, and small particles allows additional simplifications, as discussed in detail in §3.

3. Assumptions and simplifications

As noted in the introduction, particulate turbulent flows encompass a wide variety of regimes (from 'granular' to 'dilute' systems) and often suitable assumptions may be invoked to reduce the complexity of a given problem. The present study deals with volumetrically dilute suspensions ($\alpha_p \ll 1$) of very small ($\sigma < \eta$) but heavy ($\rho_p \gg \rho_f$) particles. While these conditions may appear to be rather restrictive, this class of particulate suspensions is often encountered in practice. In addition, since the simulations performed in this study neglected gravity, the turbulence (and all related correlations) remains isotropic.

The general implications of these assumptions are as follows:

(i) $\alpha_p \ll 1$ in combination with $\rho_p \gg \rho_f$ ($\alpha_p \rho_p = O(1)$) allows the neglect of particle–particle and some fluid–particle contributions to the Reynolds stress. This also implies that the RDFs can be approximated as $\tilde{g}^{ff} = \tilde{g}^{fp} = \tilde{g}^{pf} \approx 1$ with a remainder $O(\alpha_p)$.

(ii) $\sigma < \eta$ implies that variations of the correlation functions over particle volumes can be neglected to a first approximation thus eliminating the convolution integrals (shown in (30)–(33)).

The second assumption will limit the reliable range of the phase-averaged correlations to $|\boldsymbol{r}| > \sigma$ (or equivalently in Fourier space, $|\boldsymbol{k}| < 1/\sigma$); however, for the purposes of this study, this is the range of greatest interest. The resulting simplified expressions are

$$B(\boldsymbol{r}) = \left[\frac{\alpha_p}{V_p} I(r) + \alpha_p^2 \tilde{h}^{pp}(\boldsymbol{r})\right] (\rho_p - \rho_f)^2, \tag{38}$$

$$\hat{B}(\boldsymbol{k}) = \left[\frac{\alpha_p}{V_p} \hat{I}(k) + \alpha_p^2 \hat{\tilde{h}}^{pp}(\boldsymbol{k})\right] (\rho_p - \rho_f)^2. \tag{39}$$

The Reynolds stress expressions shown in (31)–(33) likewise can be reduced under the present circumstances. Under the assumptions that $\sigma < \eta$ and $\alpha_p \ll 1$, three of the RDFs can be replaced by unity and the integrals can be simplified in a manner equivalent to the density correlation yielding

$$R_{ij}^{ff}(\boldsymbol{r}) = \alpha_f^2 \rho_f \tilde{E}_{ij}^{ff}(\boldsymbol{r}) = O(1), \tag{40}$$

$$R_{ij}^{fp}(\boldsymbol{r}) = \alpha_p \alpha_f \rho_f \tilde{E}_{ij}^{fp}(\boldsymbol{r}) = O(\alpha_p), \tag{41}$$

$$R_{ij}^{pf}(\boldsymbol{r}) = \alpha_p \alpha_f \rho_p \tilde{E}_{ij}^{pf}(\boldsymbol{r}) = O(1), \tag{42}$$

$$R_{ij}^{pp}(\boldsymbol{r}) = \rho_p \frac{\overline{v_p^2}}{3} \frac{\alpha_p}{V_p} I(|\boldsymbol{r}|)\delta_{ij} + \alpha_p^2 \rho_p \tilde{g}^{pp}(|\boldsymbol{r}|)\tilde{E}_{ij}^{pp}(|\boldsymbol{r}|) = O(\alpha_p). \tag{43}$$

Furthermore, according to tensor invariance theory, the Reynolds stress tensor in isotropic turbulence can be expressed in terms of a single scalar function of r (or a single scale function of k in transform space). Consequently, one need only consider the trace of the Reynolds stress (say), rather than consider the entire nine components (Hinze 1975). Combining these approximations, we arrive at the following expression (see Sundaram 1996 for details):

$$R(r) = \alpha_f^2 \rho_f \tilde{E}^{ff}(r) + \alpha_p \alpha_f \rho_p \tilde{E}^{pf}(r), \tag{44}$$

where

$$R(r) = \tfrac{1}{2} R_{ii}(\boldsymbol{r}), \tag{45}$$

$$\tilde{E}^{ff}(r) = \tfrac{1}{2} \tilde{E}_{ii}^{ff}(\boldsymbol{r}), \tag{46}$$

$$\tilde{E}^{pf}(r) = \tfrac{1}{2} \tilde{E}_{ii}^{pf}(\boldsymbol{r}). \tag{47}$$

Fourier transforms of these results can be obtained in the standard fashion (Hinze 1975):

$$\hat{R}(k) = \alpha_f^2 \rho_f \hat{\tilde{E}}^{ff}(k) + \alpha_p \alpha_f \rho_p \hat{\tilde{E}}^{pf}(k), \tag{48}$$

where

$$\hat{\tilde{E}}^{ff}(k) = \tfrac{1}{2} \hat{\tilde{E}}_{ii}^{ff}(\boldsymbol{k}), \tag{49}$$

$$\hat{\tilde{E}}^{pf}(k) = \tfrac{1}{2} \hat{\tilde{E}}_{ii}^{pf}(\boldsymbol{k}), \tag{50}$$

For the sake of completeness, fluid–particle and particle–particle correlations and spectra may be correspondingly defined by

$$\tilde{E}^{fp}(r) = \tfrac{1}{2} \tilde{E}_{ii}^{fp}(\boldsymbol{r}), \tag{51}$$

$$\tilde{E}^{pp}(r) = \tfrac{1}{2} \tilde{E}_{ii}^{pp}(\boldsymbol{r}), \tag{52}$$

$$\hat{\tilde{E}}^{fp}(k) = \tfrac{1}{2} \hat{\tilde{E}}_{ii}^{fp}(\boldsymbol{k}), \tag{53}$$

$$\hat{\tilde{E}}^{pp}(k) = \tfrac{1}{2} \hat{\tilde{E}}_{ii}^{pp}(\boldsymbol{k}). \tag{54}$$

4. Direct numerical simulations

This study is concerned with the motion of heavy particles in a turbulent, suspending medium. Given that present methods of forcing interfere with the spectral dynamics in some unknown manner, it was decided to restrict this study to freely decaying, isotropic turbulence. This does introduce additional complications in the form of time-dependent turbulence properties. However, it is expected that after a suitable equilibration period, and well before the limit of weak turbulence sets in, it will be possible to observe the intrinsic modulation of turbulence by particles, independent of the initial conditions.

Gravity is neglected to preserve the isotropic nature of the problem and for the sake of simplicity. Note that in the presence of gravity, the ensuing settling-induced relative motion can cause turbulence production (Elghobashi & Truesdell 1993). In this case, particle potential energies would have to be accounted for in addition to particle and fluid kinetic energies in the energy balance. Particles in our simulations owe their motion to initialization and fluid turbulence alone.

4.1. *Particle motion*

The motion of discrete particles in a suspending fluid has been studied quite extensively. Maxey & Riley (1983) derived the full particle equation of motion under the conditions $\sigma \ll \eta$ and $\sigma \Delta u/\nu \ll 1$ where Δu is the characteristic velocity difference between the particle and local fluid. Particles are also assumed to be sufficiently large that any Brownian or non-continuum motion of the particles may be neglected (i.e. infinite Péclet number). The governing equations for the nth particle are then given by

$$\frac{\mathrm{d}\boldsymbol{x}^n}{\mathrm{d}t} = \boldsymbol{v}^n, \tag{55}$$

$$\frac{\mathrm{d}\boldsymbol{v}^n}{\mathrm{d}t} = \frac{\boldsymbol{u}(\boldsymbol{x}^n) - \boldsymbol{v}^n}{\tau_p} + \sum_{j \neq n} \boldsymbol{a}^{nj}, \tag{56}$$

where

$$\tau_p \equiv \frac{\rho_p \sigma^2}{18\mu}, \tag{57}$$

$\boldsymbol{x}^n$ and $\boldsymbol{v}^n$ denote the instantaneous position and velocity of the nth particle centre and τ_p, referred to as the particle response time, is a measure of particle inertia. $\boldsymbol{a}^{nj}$ represents the instantaneous acceleration of the nth particle due to an elastic (i.e. momentum and energy conserving) collision with the jth particle. The assumption of linear drag is valid under the condition that $\sigma \Delta u/\nu < 1$ and $\rho_p/\rho \gg 1$ (Maxey & Riley 1983). In view of the low particle Reynolds numbers encountered, inclusion of nonlinear drag was deemed unnecessary. Particles obey periodic boundary conditions.

Since particles are not restricted to lie on the fluid grid points or vertices an interpolation function, S, is needed to estimate fluid velocities at the particle centres. The interpolation function has the following general form:

$$\boldsymbol{u}(\boldsymbol{x}^n) = \sum_v S(\boldsymbol{x}^n, \boldsymbol{x}^v)\boldsymbol{u}(\boldsymbol{x}^v), \tag{58}$$

where $\boldsymbol{x}^v$ represents a fluid vertex or grid point. The function chosen for the forward interpolation is a piecewise cubic Lagrangian polynomial.

Another novel aspect of these simulations is the implementation of direct particle interactions modeled as hard-sphere elastic collisions. A detailed description of the principles and algorithm used to compute particle collisions is provided in Sundaram & Collins (1996). This study uses the same method to resolve contact and advance the particles.

4.2. *Fluid motion*

The fluid phase is governed by the incompressible Navier–Stokes equations. Even though the direct influence of the particles on the continuity equation is neglected, in view of the extremely low volumetric loadings, the effect on the fluid momentum is

accounted for. The resulting equations are

$$\nabla \cdot \boldsymbol{u} = 0, \tag{59}$$

$$\frac{\partial \boldsymbol{u}}{\partial t} + \boldsymbol{u} \cdot \nabla \boldsymbol{u} = -\frac{\nabla P}{\rho_f} + \nu \nabla^2 \boldsymbol{u} - \frac{1}{\rho_f} \sum_{n=1}^{N_p} m_p \frac{(\boldsymbol{u}(\boldsymbol{x}^n) - \boldsymbol{v}^n)}{\tau_p} \delta(\boldsymbol{x} - \boldsymbol{x}^n), \tag{60}$$

where $m_p \equiv \rho_p V_p$ is the particle mass. The last term on the right-hand side of (60) is the force exerted by the particles on the fluid. Once again, since this force is computed at the particle centres, we must model the particle force at the grid vertices where the fluid field is updated. The discretized particle source term is given by

$$\sum_{n=1}^{N_p} \frac{\rho_p V_p}{\rho_f V_g} \frac{(\boldsymbol{u}(\boldsymbol{x}^n) - \boldsymbol{v}^n)}{\tau_p} S^*(\boldsymbol{x}^n, \boldsymbol{x}^v) \tag{61}$$

where V_g is the volume of fluid being updated and $S^*(\boldsymbol{x}^n, \boldsymbol{x}^v)$ is the 'reverse' or 'backward' interpolation function. Recall from (58) that the particle update requires a 'forward' interpolation of the fluid velocity to the particle position ($S(\boldsymbol{x}^n, \boldsymbol{x}^v)$). For proper conservation of the total energy, Sundaram & Collins (1996) have shown that the reverse interpolation of particle source should be the same as the forward interpolation; hence, an identical cubic Lagrangian polynomial is used for both the forward and backward interpolations.

The Navier–Stokes equations are discretized on a 128^3 cubic grid. Periodic boundary conditions are imposed and there is no mean flow. The fluid velocity is updated using a pseudo-spectral algorithm similar to the one described in Canuto *et al.* (1988). Partial dealiasing is accomplished by zeroing wavenumbers beyond $8/9\ k_{max}$ as originally suggested by Orszag & Patterson (1972). Time advancement is done using an efficient fourth-order Runge–Kutta scheme.

4.3. *Parameters*

The physical parameters that characterize the particles are number, N_p, diameter, σ, and density, ρ_p, although it is convenient to replace the density by the particle response time, τ_p, defined in (57). The particle response time arises naturally from the dynamic equations and is therefore the true measure of the particle inertia. This time can be non-dimensionalized using any of the turbulence time scales. However, anticipating the importance of the small scales, we choose to non-dimensionalize with the Kolmogorov time scale. Thus, a particle Stokes number is defined as

$$St = \frac{\tau_p \epsilon^{1/2}}{\nu^{1/2}}. \tag{62}$$

We are interested in particle Stokes numbers that are initially of order unity. For aerosol systems with particle–fluid density ratios that are on the order of 1000, the corresponding Reynolds numbers are appropriately small. A physical system that corresponds to this condition would be, for example, 100 μm particles ($\rho_p = 1000$ kg m^{-3}) suspended in air at standard conditions ($\rho_f = 1$ kg m^{-3}, $\mu = 2 \times 10^{-5}$ kg m^{-1} s^{-1}) with turbulent energy dissipation rates (ϵ) in the range of 0.1–1.0 W kg^{-1}. Conditions such as these are easily achieved in pneumatic pipe flows.

Two other dimensionless parameters are required to complete the description of the particles. We choose the volumetric and mass loadings of the particles. In general, the mass loadings (ϕ_p) were appreciable ($\sim 10\%$) whereas the volumetric loadings (α_p) were kept small so that the simulations were well within the dilute limit ($\sim 10^{-4}$).

Parameter	F1	F2
L	2π	2π
$u'(0)$	0.9362	0.9362
$\epsilon(0)$	0.22282	0.19182
ρ_f	1.0	1.1616
ν	7.854×10^{-3}	6.761×10^{-3}
$l_e(0)$	1.6223	1.6223
$T_e(0)$	1.7328	1.7328
$\eta(0)$	0.0384	0.035629
$\tau_\eta(0)$	0.18774	0.18774
$\lambda(0)$	0.68074	0.68074
$Re_\lambda(0)$	81.145	94.258
$k_{max}\eta(0)$	2.1845	2.027
Δt	0.0031	0.0031

TABLE 1. Listing of turbulence parameters for the two fluid runs used in the study. F1 is the base, unladen fluid computation. F2 denotes a fluid laden with infinitesimal particles at an identical mass loading, simulated as a fluid with a higher effective density. The other parameters are defined as follows: L is the box size; $u'(0)$ is the initial turbulence intensity; $\epsilon(0)$ is the initial turbulence dissipation rate per unit mass; ρ_f is the fluid density; ν is the fluid kinematic viscosity; $l_e(0)$ is the initial integral length scale; $T_e(0)$ is the initial large eddy turnover time; $\eta(0)$ is the initial Kolmogorov eddy length scale; $\tau_\eta(0)$ is the initial Kolmogorov eddy time scale; $\lambda(0)$ is the initial Taylor microscale; $Re_\lambda(0)$ is the initial turbulence Reynolds number based on the Taylor microscale; $k_{mas}\eta(0)$ is the initial resolution of the calculation; and Δt is the time increment. All dimensional quantities are expressed in arbitrary units.

Two parametric studies were carried out. The first was designed to isolate the effect of Stokes number while fixing the volumetric and mass loadings. This was accomplished by varying both the particle diameter and particle number density simultaneously, in such a manner that the product $N_p\sigma^3$ was constant. In addition, a limiting solution for the case of $\sigma \to 0$ ($N_p \to \infty$) was sought. In this limit, we assume that the 'particles' behave precisely like fluid elements, on account of their size, and so the particle–fluid system reduces to a pure fluid with an appropriately elevated density (to account for the mass of particles), but unaltered molecular viscosity (owing to the low volume fraction of particles). This conceptual argument, beyond being intuitively satisfying, is at least partially supported by recent numerical simulations by Nitsche & Batchelor (1997). They looked at the motion of a spherical blob, consisting of a viscous fluid embedded with a large number of tiny particles, as it fell through the pure fluid under gravity. Their simulations showed that in the limit of a large number of small particles the motion of the blob closely resembled the expected motion of an immiscible drop with an appropriately elevated density and no surface tension.

The second study considers the effect of varying the volumetric and mass loadings while fixing the Stokes number. This was accomplished by varying the number of particles with a fixed density and diameter (and hence response time). Thus, the dynamic properties of each particle was fixed so as to isolate the effect that loading has on the system.

4.4. *Organization of computations*

The fluid turbulence properties and scales at the start of each simulation are enumerated in table 1. Fluid run F1 is the unladen fluid used as the base fluid case for the investigation. The augmented-density fluid run (simulating the system loaded with

Phenomenon	Index	τ_p/T_e	τ_p/τ_η	σ/η	N_p	ρ_p/ρ_f	α_p ($\times 10^4$)	ϕ_p
Inertia study	A	0.17	1.60	0.18	262 144	900	1.80	0.14
	B	0.35	3.20	0.26	89 915	900	1.80	0.14
	C	0.69	6.41	0.36	32 768	900	1.80	0.14
Loading study	D	0.35	3.20	0.18	262 144	1800	1.80	0.24
	F	0.35	3.20	0.18	89 915	1800	0.6	0.1
	G	0.35	3.20	0.18	32 768	1800	0.2	0.04

TABLE 2. Listing of the fundamental and re-expressed particle parameters for the various runs used in the study. Note that τ_p/τ_η is referred to as the Stokes number in the text; σ/η is the dimensionless particle diameter; N_p is the total number of particles; ρ_p/ρ_f is the particle-to-fluid density ratio; and α_p and ϕ_p are the volume and mass fraction of particles respectively. All fluid length and time scales are based on their initial value.

vanishingly small particles) is denoted by F2. Table 2 provides a listing of the particle runs and associated parameters used in this study. Particle-laden computations are indexed A, B, C, D, F, G. Runs (F2, A, B, C) constitute the Stokes number study, while the loading study includes runs (F1, D, F, G).

The initial fluid field was obtained from a stationary forced run. Particles were initially placed in random, non-contact positions and assigned fluid velocities to begin with. The time required for the particles to equilibrate with the fluid from this initialization is a function of their inertia or Stokes number. The mean-square slip velocity (which is proportional to the dissipation due to particle drag) provides a measure of the adjustment between the two phases. The point in time at which the drag dissipation begins to decrease is indicative of the attainment of equilibrium. As will be seen later, all particle runs achieved equilibrium by approximately one eddy turnover time. The combined systems were time advanced up to approximately four eddy turnover times at which point the turbulence in the particle-loaded cases had decayed to $Re_\lambda \approx 20$ (see figure 1).

5. Particle and fluid kinetic energy

In this section we present results for the total kinetic energy of the particle and fluid phases defined respectively as

$$T_f \equiv \frac{1}{2}\int_V \rho_f u^2 \,\mathrm{d}V = \tfrac{1}{2}\rho_f \overline{u^2} V \tag{63}$$

and

$$T_p \equiv \tfrac{1}{2} m_p \sum_{n=1}^{N_p} (v^n)^2 = \tfrac{1}{2} m_p \overline{v^2} N_p, \tag{64}$$

where V is the total volume of the system and $\overline{u^2}$ and $\overline{v^2}$ are the average fluid and particle kinetic energies respectively. The integral in (63) is evaluated approximately by summing over all of the grid points in the system. For an isotropic and periodic particulate system, the exact dynamic equation for the total fluid kinetic energy can be shown to be (Sundaram & Collins 1996)

$$\frac{\mathrm{d}T_f}{\mathrm{d}t} = -\Phi_v - \sum_{n=1}^{N_p} \frac{m_p \boldsymbol{u}(\boldsymbol{x}^n)\cdot[\boldsymbol{u}(\boldsymbol{x}^n) - \boldsymbol{v}^n]}{\tau_p}, \tag{65}$$

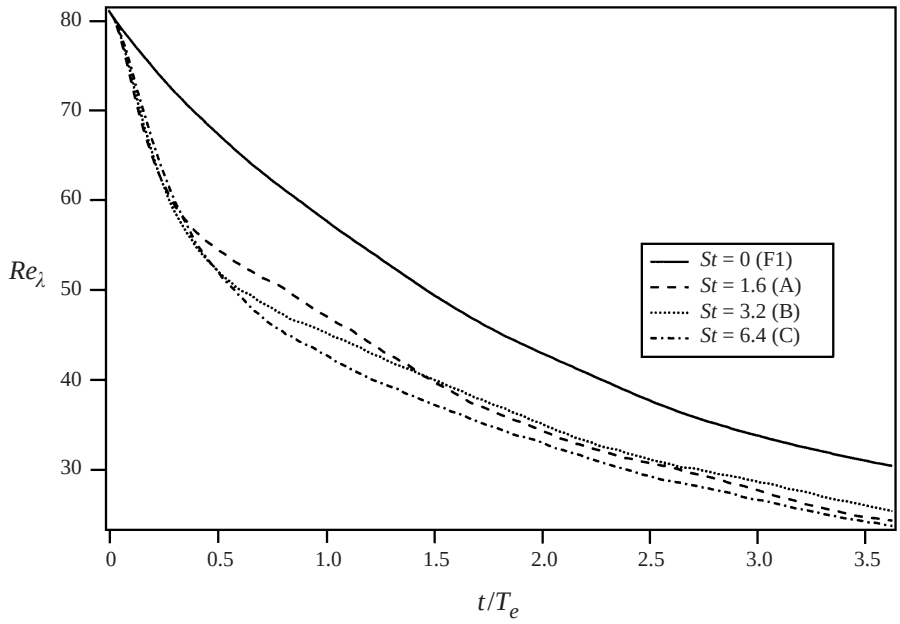

FIGURE 1. Decay of turbulence Reynolds numbers based on the Taylor microscale, Re_λ, for various Stokes numbers St. Computations are continued until a weak turbulence limit of $Re_\lambda \approx 25$ is reached.

where

$$\Phi_v \equiv \int_V \rho_f \epsilon \, \mathrm{d}V \tag{66}$$

and

$$\epsilon \equiv \nu \left(\nabla \boldsymbol{u} + \nabla \boldsymbol{u}^T\right) : \nabla \boldsymbol{u}. \tag{67}$$

The total particle-phase kinetic energy is given by

$$\frac{\mathrm{d}T_p}{\mathrm{d}t} = \sum_{n=1}^{N_p} \frac{m_p \boldsymbol{v}^n \cdot [\boldsymbol{u}(\boldsymbol{x}^n) - \boldsymbol{v}^n]}{\tau_p}. \tag{68}$$

Note that particle collisions play no role in the total particle kinetic energy since they are elastic and thus conserve the total kinetic energy of the colliding pair. Summing (65) and (68) yields an expression for the total kinetic energy of the system, $T_t \equiv T_f + T_p$:

$$\frac{\mathrm{d}T_t}{\mathrm{d}t} = -\Phi_v - \Phi_p, \tag{69}$$

where

$$\Phi_p \equiv \sum_{n=1}^{N_p} \frac{m_p \left[\boldsymbol{u}(\boldsymbol{x}^n) - \boldsymbol{v}^n\right]^2}{\tau_p}. \tag{70}$$

Notice that the total kinetic energy of the system is dissipated by two mechanisms: (i) viscous dissipation occurring throughout the continuous fluid phase (Φ_v); and (ii) losses due to drag at the particle interfaces (Φ_p). Thus, particles are manifestly dissipative to the total kinetic energy of the system.

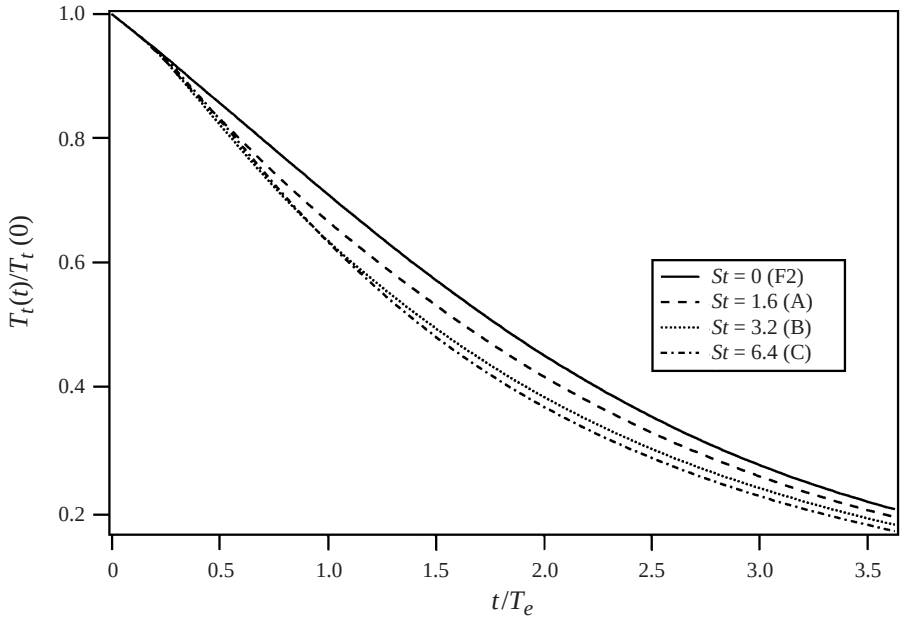

FIGURE 2. Evolution of the normalized total kinetic energies (i.e. fluid + particle) with time. Increase in particle Stokes number is seen to lower the total energies.

Several earlier studies (Squires & Eaton 1990; Elghobashi & Truesdell 1993) have considered the effect that the particles have on the fluid-phase kinetic energy. Here the question is more subtle because there is a continuous exchange of energy between the two phases that is governed by the relative magnitudes of $\overline{u^2}$, $\overline{\boldsymbol{u}\cdot\boldsymbol{v}}$ and $\overline{v^2}$. Once the particles have had sufficient time to equilibrate, it is observed that

$$\overline{u^2} \geqslant \overline{\boldsymbol{u}\cdot\boldsymbol{v}} \geqslant \overline{v^2} \tag{71}$$

implying that for particle systems at equilibrium and in the absence of body forces or mean-flow gradients, the fluid phase continuously loses energy while the particles gain energy from the drag interaction; however, (69) ensures that the loss from the fluid exceeds the gain by the particles, resulting in a net loss of energy from the system. It must be emphasized that these results apply to equilibrium systems only, and indeed they potentially may be reversed under the following circumstances:

(i) particles obtain energy from a source other than the fluid (for example, from gravity or due to the initial conditions);

(ii) if there are mean shear production terms present, the presence of particles may subtly alter the production–dissipation balance, again possibly leading to an increase in the fluid turbulent energies.

Recall that the Stokes number study includes the fluid run (F2) and the three particle runs A, B and C. This study is designed so that the total mass of each system is identical. Likewise, the total energy of each system, T_t, is initialized to the same value. Figure 2 shows the behaviour of T_t as a function of time (normalized by its initial value). As suggested by (69), the presence of particles increases the rate of dissipation of kinetic energy in the system. Furthermore, the degree of energy suppression increases monotonically with increasing Stokes number. The explanation for this trend is deferred until after the discussion of dissipation mechanisms has been completed.

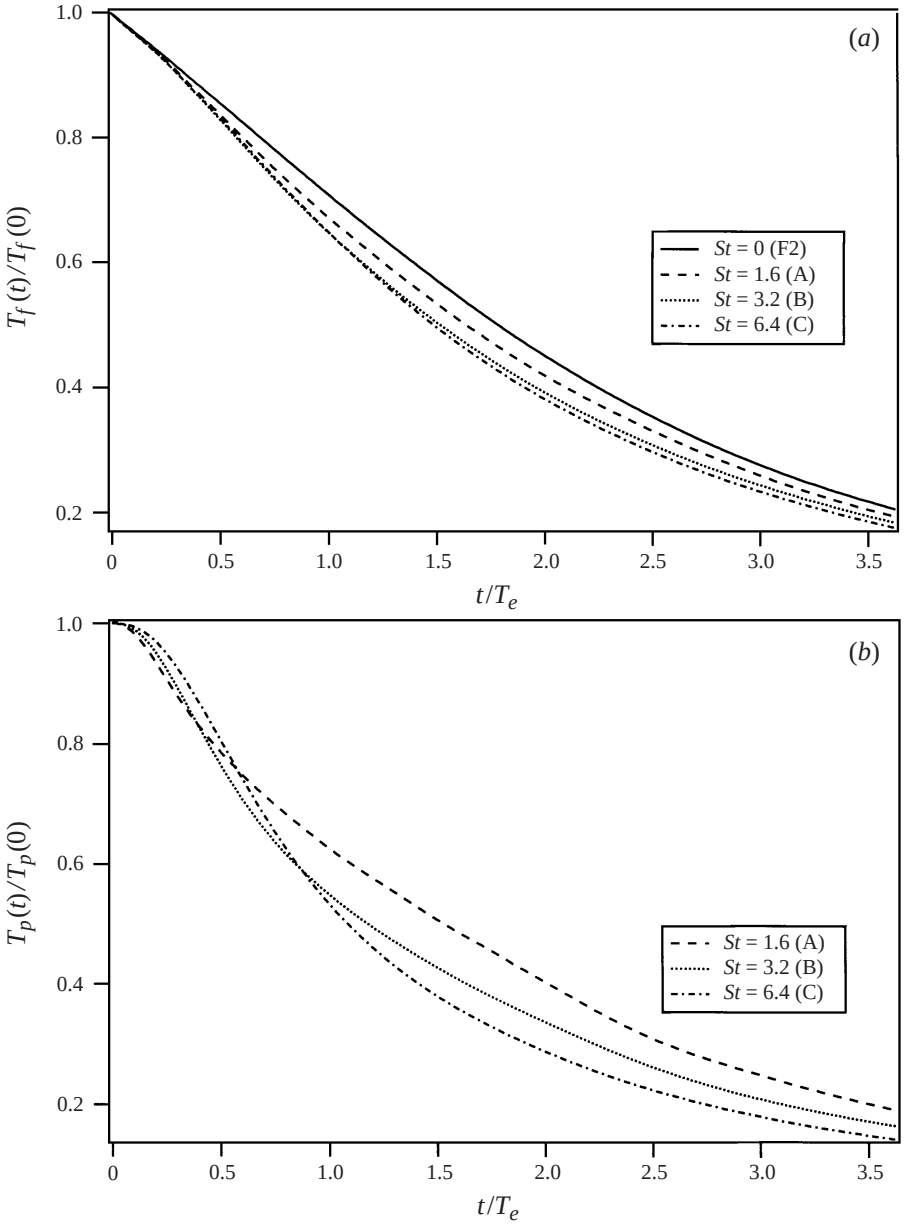

FIGURE 3. (*a*) Fluid turbulent kinetic energy as a function of time at three different Stokes numbers. Notice that the energy is suppressed with an increase in St. (*b*) Particle kinetic energy as a function of time. At long times, they show a similar trend.

Figure 3(*a*) shows the fluid turbulent kinetic energies normalized by their initial value. The trend observed here is identical to that found for the total kinetic energy. As noted above, the net effect of the particles (at equilibrium) is to reduce the fluid energy. This effect is also expected to grow with increasing Stokes number. The particle energy (see figure 3*b*), on the other hand, is only observed to obey the preceding trends at

long times, while the behaviour at short times is reversed. We believe this cross-over at early times occurs because the particles still retain some memory of their initial velocity. Recall that the particles were initially given velocities equal to the local fluid velocity. However, because of their increased inertia, the equilibrium energy for the particles is below that of the fluid (see (71)). This suggests that initially the particles are not in equilibrium with the fluid, and furthermore, their degree of disequilibrium increases with Stokes number. Thus, the short-time behaviour in figure 3(*b*) reflects the non-equilibrium initial conditions, while the long-time behaviour follows the expected trends.

The rates of dissipation of energy due to viscous forces (Φ_v) and the presence of particles (Φ_p) are plotted in figures 4(*a*) and 4(*b*) respectively. Both curves are normalized by the initial value of the viscous dissipation rate ($\Phi_v(0)$) for convenience. At short times, the viscous dissipation rate is strongly influenced by the presence of the particles. The explanation is related to the well-known pivot in the fluid energy spectrum induced by the exchange of energy with the particles (Squires & Eaton 1990; Elghobashi & Truesdell 1993). As will be seen later, the pivot shifts energy from low to high wavenumbers (i.e. from large to small length scales), thereby increasing the overall dissipation rate. The degree of pivoting increases with Stokes number, which explains why the peak in the rate of viscous dissipation also increases with Stokes number. At long times, the trend reverses because at high Stokes number the fluid energy is dissipated to such a degree that the local dissipation rate is ultimately reduced. Section 7 will consider the pivoting of the energy spectrum in greater detail.

The second dissipation rate arising from the particles, Φ_p, is shown in figure 4(*b*). Since this dissipation is proportional to the velocity difference between the particles and fluid, its value is initially zero. It then increases to a maximum before decaying. The location of the maximum shifts to longer times with increasing Stokes number indicating a slower equilibration process; however, it is more difficult to interpret the magnitude of the maximum on account of the decaying energy levels of both phases. Notice also that at long times, after the particles have had time to equilibrate, the three curves are nearly identical. This implies that although the rate of dissipation of energy by particles is perhaps a strong function of the mass loading of particles, it is relatively insensitive to the particle Stokes number. By considering (71), the convergence of the curves in figure 4(*b*) suggests that once the particles have settled into equilibrium, $\overline{(\boldsymbol{u}-\boldsymbol{v})^2} \propto \tau_p$, over the limited range of particle St considered.

An important question to consider is how the fluid response is related to the particle loading. The loading study (F1, D, F and G) consists of a series of runs where the particle properties are fixed while the number of paricles (and hence both the volume and mass loadings) are varied. We include, for the sake of comparison, a single-phase fluid computation which corresponds to setting the number of particles to zero.

Figure 5(*a*) shows the excess viscous dissipation ($\Delta\Phi_v = \Phi_v - \Phi_v^{F1}$) normalized by the initial viscous dissipation and the mass loading. The curves normalized in this fashion collapse together suggesting that the contribution from each individual particle is nearly same. The equivalent curves for the particle dissipation, presented in figure 5(*b*), show a similar trend. We therefore conclude that at the concentrations considered in this study, each particle acts independently, and thus their collective effect scales linearly with their total number, N_p. We anticipate that such a simplistic scaling would not be valid at higher particle loadings.

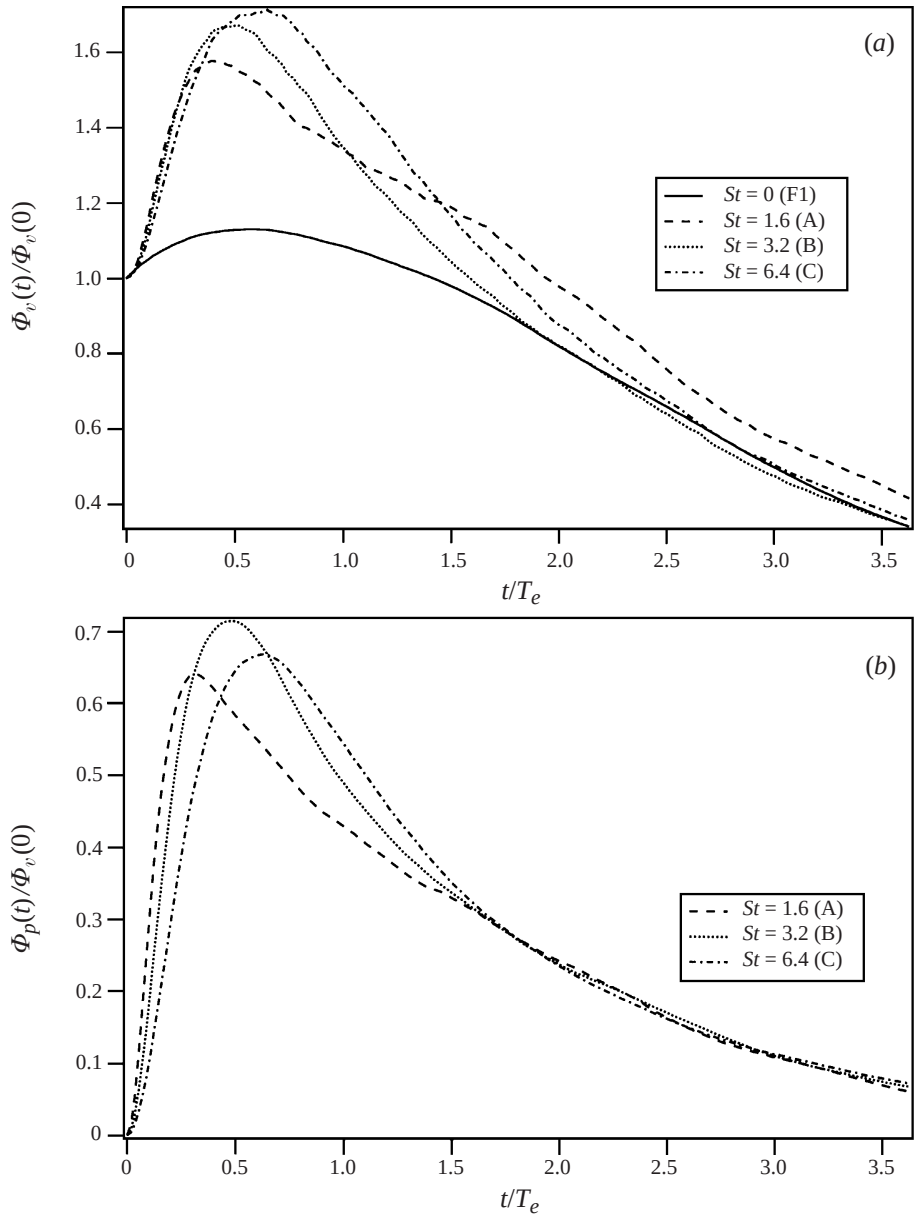

FIGURE 4. (*a*) Total dissipation of turbulent energy by viscous forces. An increase in particle Stokes number is seen to enhance the viscous dissipation in the fluid phase. The crossover at long times is believed to be related to the varying total energies remaining in the system at long times. (*b*) Particle drag dissipation as a function of time. Notice that they are almost identical at long times (i.e. beyond the equilibration).

6. Two-point density correlation

We begin our discussion of two-point statistics by considering the density correlation, $B(r)$, defined in (38). The density correlation is related to two functions, the Overlap function $I(r)$ which depends solely on the particle shape, and the radial distribution function $\tilde{h}^{pp}(r)$ which describes statistically the spatial distribution of the

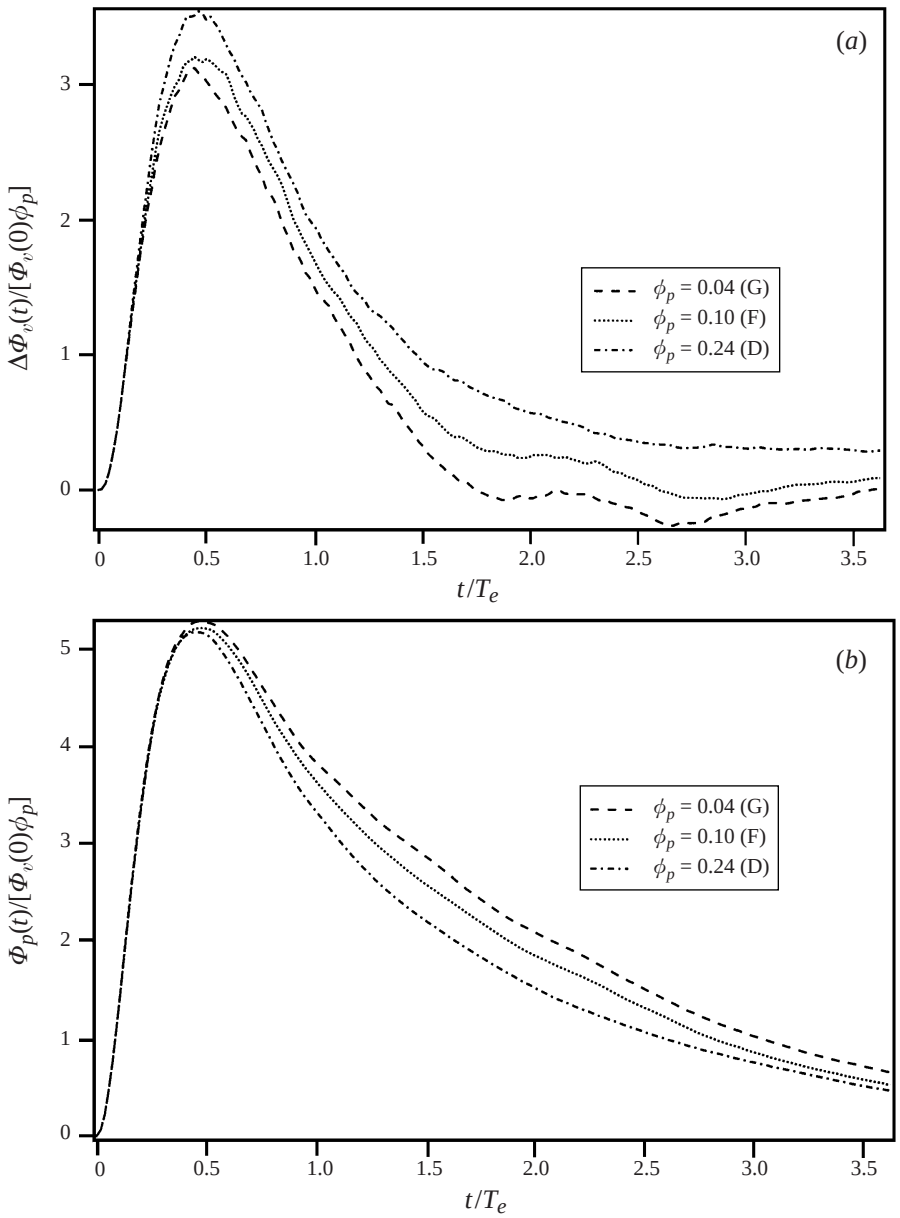

FIGURE 5. (*a*) Excess viscous dissipation rate (due to the presence of particles, $\Delta\Phi_v = \Phi_v - \Phi_v^{F1}$) and (*b*) particle drag disspation rate normalized by the particle loading. The collapse of the curves in both plots indicates a linear scaling with the number of particles, N_p.

particles (see §2 for details). This section discusses the results obtained from the DNS. All correlations (spectra) were obtained after approximately two eddy turnover times (unless specified otherwise). This time was chosen because sufficient time had elapsed so that the particles had achieved equilibrium with the fluid, yet the turbulence had not decayed to the weak-turbulence limit. Although correlations (spectra) at later times differ quantitatively from those presented here, the trends and qualitative behaviour remain unaffected.

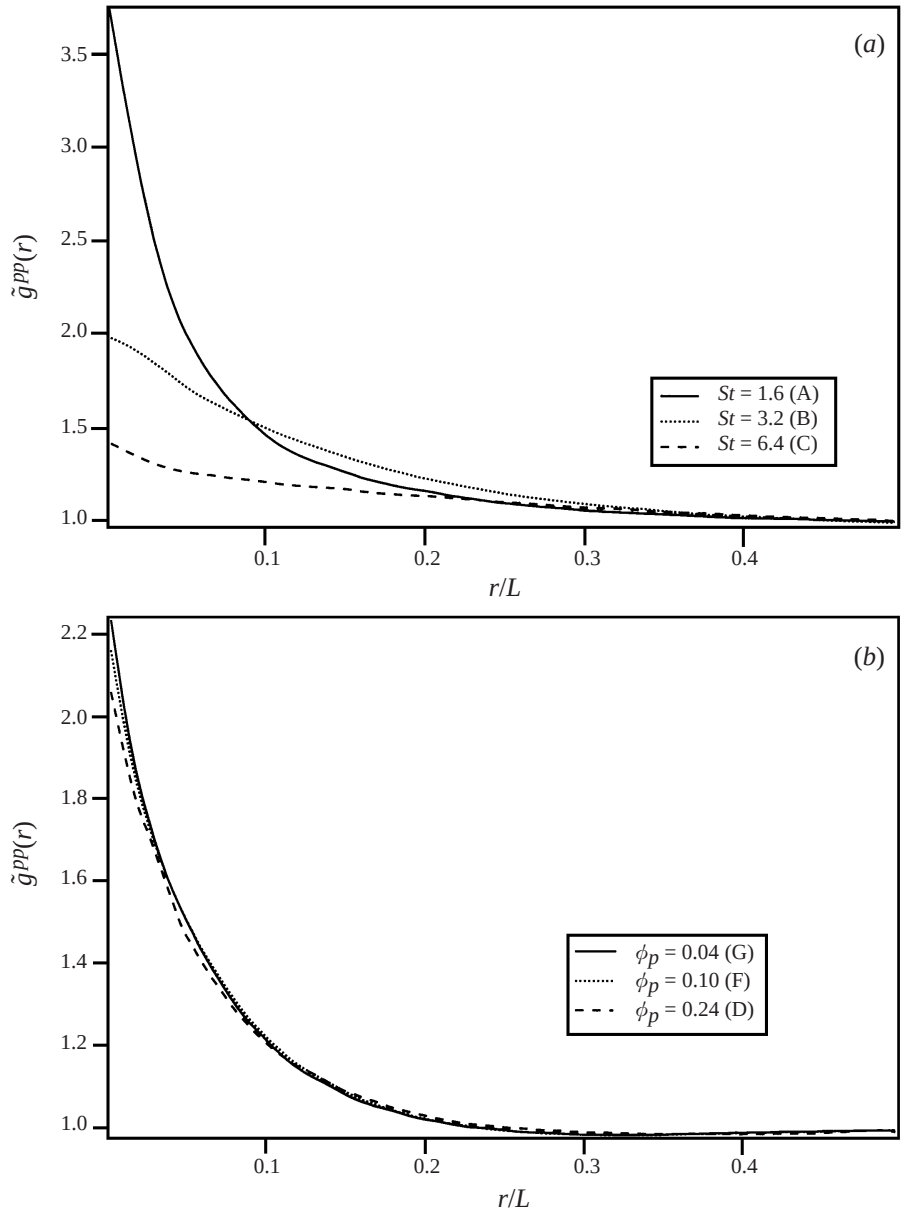

FIGURE 6. The radial distribution function as a function of r ($r > \sigma$) at different (a) particle Stokes numbers, and (b) particle loadings. As has been observed in previous studies, the RDF is very sensitive to the Stokes number and relatively insensitive to the loading (assuming it remains in the dilute regime). The small effect of loading that is observed is due to particles excluding others in their immediate neighbourhood.

Figure 6(a) shows the radial distribution function (RDF), $\tilde{g}^{pp}(r)$, for runs A, B, and C. It is known that for a uniformly distributed hard-sphere system, the maximum value of the RDF can be approximated by

$$\tilde{h}^{pp}(r \sim \sigma) = \frac{1 + \alpha_p}{(1 - \alpha_p)^3} - 1 = O(\alpha_p). \tag{72}$$

Bearing in mind that volume concentrations are $O(10^{-4})$, from the results shown in figure 6(*a*), it is readily apparent that the particles are not uniformly distributed. Furthermore, the degree of non-uniformity decreases with increasing Stokes number over the range of Stokes numbers considered. The effect results from a phenomenon known as preferential concentration, whereby particles, owing to their higher inertia, are flung from regions of high vorticity and collect in regions of low vorticity (Maxey 1987; Squires & Eaton 1991). The increase in particle concentration in these low-vorticity regions causes the RDF to increase at small r, compared to the randomly distributed case. The result is qualitatively similar to an earlier study based on one-way coupling (Sundaram & Collins 1997).

It is interesting to note that the RDF must satisfy the following integral constraint (conservation of particles) :

$$\int_V \tilde{g}^{pp}(r)\, \mathrm{d}\boldsymbol{r} = \frac{N_p - 1}{N_p} V \approx V. \tag{73}$$

This integral constraint necessitates a crossover between the various curves, as can be seen in figure 6(*a*).

Figure 6(*b*) shows the corresponding dependence on the particle loading (runs D, F, and G). Notice the relative insensitivity of the RDF to the loading. This had been observed in a previous study (Sundaram & Collins 1997) and is related to the relatively dilute conditions under investigation. Corrections to the RDF for particle volume exclusions should scale like $O(\alpha_p)$, which is small. The somewhat larger variation seen in figure 6(*b*) is most likely due to statistical differences in the fluid state at the time of comparison.

It is often useful to consider the Fourier transform of the correlations in order to gain some understanding of the different length scales of the fluid motion that affect the density correlation. Unlike the calculation of the energy spectrum, which can be accomplished by taking advantage of the spectral representation used in the numerical method, the transform of the RDF must be accomplished by directly transforming the RDF itself. This is a troublesome calculation because of the inherent statistical noise in the RDF. Mild statistical noise in the original data set can lead to substantial noise in the resulting Fourier transform, thus some smoothing is required (Sundaram 1996).

Figure 7 shows the three-dimensional Fourier transform of the RDF. It appears that the maximum in each curve increases in magnitude and shifts slightly to higher wavenumbers with decreasing Stokes number. It was argued in an earlier study (Sundaram & Collins 1994*a*) that an outward shift in these spectra was the result of a decrease in the mean separation distance between neighbouring particles. As this comparison is being made at a constant volume loading, this can only imply variations in the degree of preferential concentration. Also, note that for non-penetrating particles $\tilde{h}^{pp}(0) = -1$ which implies that all corresponding spectra must integrate to -1. At first glance, it may appear odd that these curves do not cross the zero axis; however it must be recalled that the curves shown in figure 7 are only valid over the range $0 < k \ll 1/\sigma$. Apparently the curves cross the axis at very high wavenumbers; unfortunately, that behaviour cannot be observed since it requires information about the RDF at small separation distances, which is precisely where the signal-to-noise ratio is very small.

The corresponding density correlation spectrum is presented in figure 8(*a*). The maxima observed in the RDFs can now be seen in the density correlations as well,

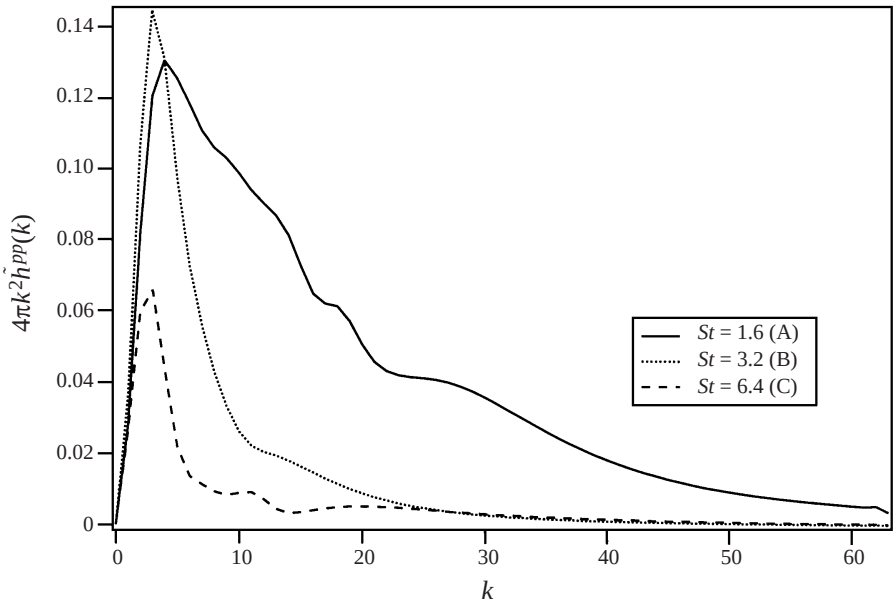

FIGURE 7. The three-dimensional Fourier transform of $\tilde{h}^{pp} = \tilde{g}^{pp} - 1$ is shown as a function of wavenumber k ($k < 1/\sigma$). The shift in the maximum towards higher wavenumbers and the larger tail with decreasing Stokes number is indicative of growing preferential concentration.

although now the curves are seen to rise again at high wavenumbers. The cause of this second increase is the Overlap function, which in Fourier space is dominant at high wavenumbers. Figure 8(*b*) shows the same density spectra over a much larger range of wavenumbers. At high wavenumbers, the three curves collapse into a single curve defined by the Overlap function. Furthermore, the initial peaks in the curve seen in figure 8(*a*) are now completely obscured by the much larger oscillations from the Overlap function.

In a particle–fluid system, it can be intuitively understood that there are two different sources for density fluctuations. One is the variation between particle and fluid densities, occurring at the particle surface. This action occurs over scales corresponding to the particle size and can be termed *static B*. The other major source of density fluctuations is due to changes in the relative spatial distribution of the particles. This component, referred to as the *dynamic B* typically occurs over much larger fluid dynamic scales.

Note that in gas–solid flows at high density ratios, the static component is many orders of magnitude larger than the dynamic component. This fact is readily apparent in figure 8. Furthermore, although the fraction of total B (see (21)) contributed by the static component is substantial, it is the dynamic B that ultimately impacts the turbulence. This is a troublesome problem for single-point models that, by definition, cannot distinguish between the static and dynamic components. Indeed, single-point models must often artificially reduce the value of total B so that it more closely resembles the dynamic B contribution (Besnard, Harlow & Rauenzahn 1987). This again highlights the significant advantage gained by utilizing two-point statistics to analyse and/or model particle-laden turbulent flows.

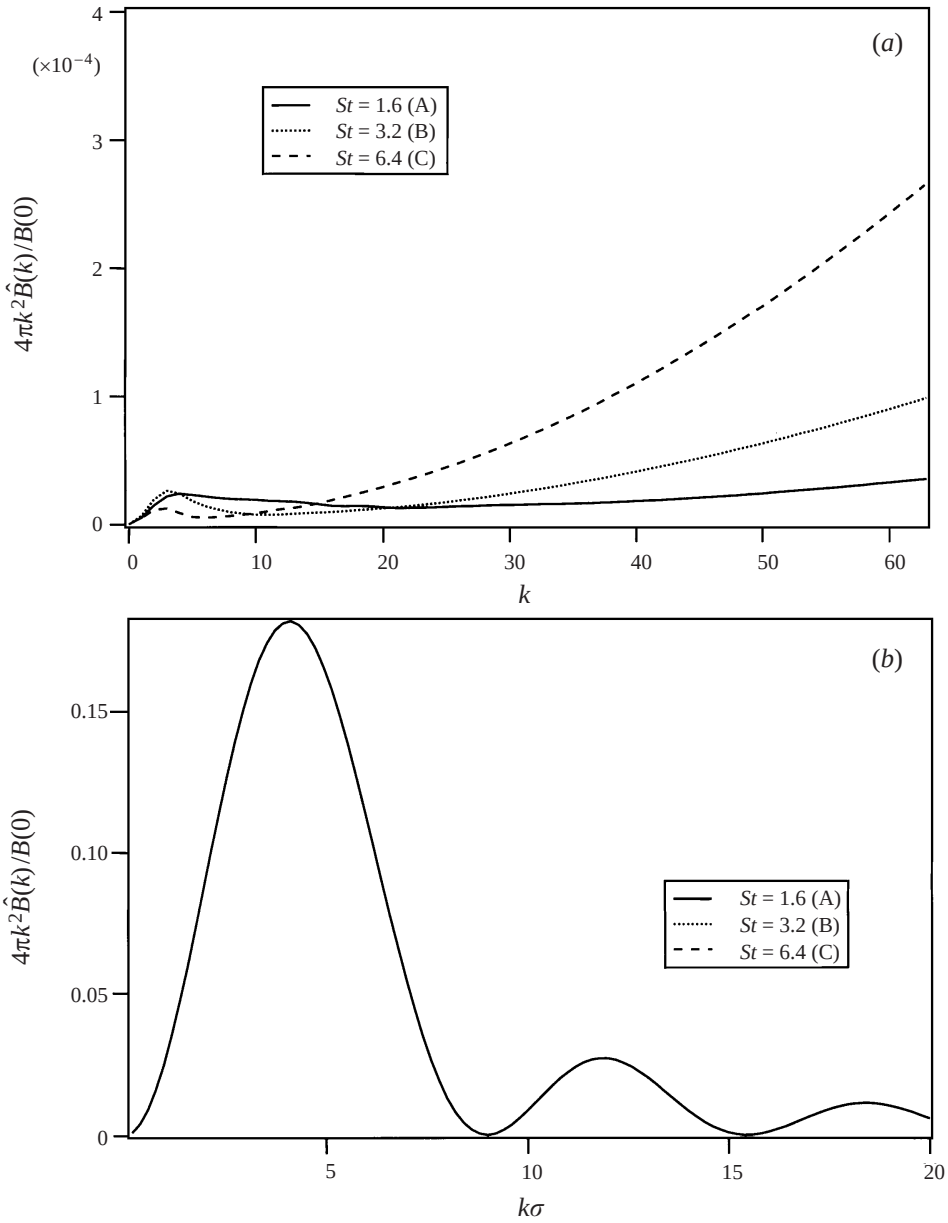

FIGURE 8. (*a*) The density correlation as a function of k at different particle Stokes numbers. All dynamic information (pertaining to the changing RDF) is contained within the first 20 wavenumbers. Thereafter the curves are dominated by the Overlap function. This is evident in (*b*) which shows the same correlation over a much larger range of wavenumbers. The initial peak caused by the RDF is now completely obscured by the much larger oscillations from the Overlap function.

7. Two-point Reynolds stress

We begin the discussion of the energy correlations by comparing the three component correlations (fluid–fluid, fluid–particle, and particle–particle) from a typical run. Although the results from any given run are functions of the parameter values, the

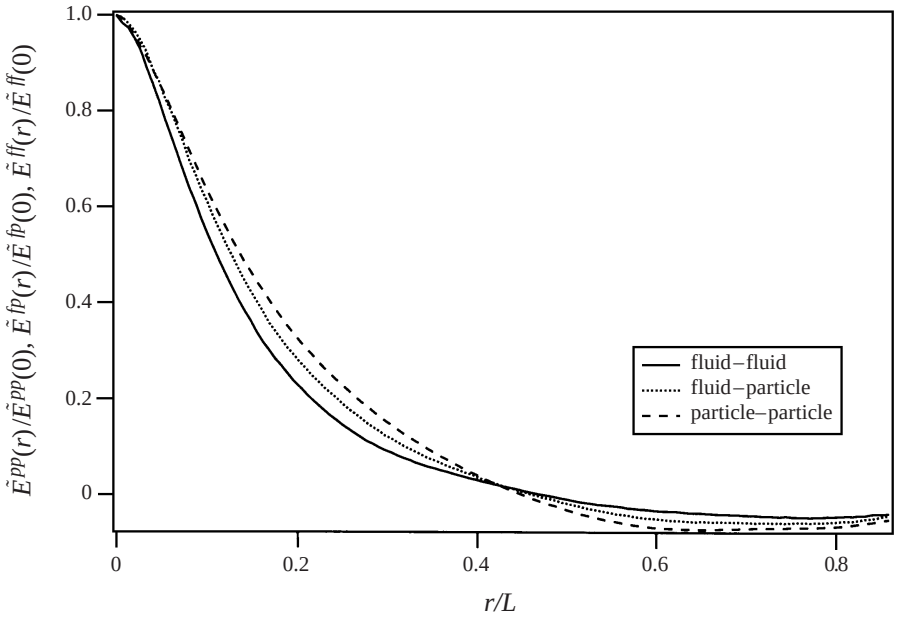

FIGURE 9. Comparison of the three component correlations from run B ($r > \sigma$). The ordering at small r is a consequence of the Schwarz inequality and the fact that the particles contain less energy than the fluid. Notice that the particles are more strongly correlated at intermediate distances than the fluid.

qualitative features of the correlations and spectra remain the same. Figure 9 shows a comparison of the three component correlations from run B with particle Stokes number value of 3.2. Notice that the fluid correlation is relatively strong at small distances, but then drops off more quickly than the particle–fluid and particle–particle correlations. This suggests that the inclusion of particles increases the correlation length relative to the pure fluid. A plausible physical argument for the increase in the correlation length is as follows. Consider two initially correlated but separating particles and two equivalent fluid elements. Upon separating a moderately large distance r (say) the particles, having greater inertia than the fluid, will remain relatively unaffected (i.e. , more strongly correlated) by their new fluid mechanical environment than the equivalent fluid elements. Hence particles remain correlated over greater lengths than fluid elements.

Figure 10 shows the total energy correlation for the three values of the Stokes number and the fluid run corresponding to $St = 0$ (Runs A, B, C and F2). Notice that the correlation length increases monotonically with increasing Stokes number. This visual trend is confirmed by the integral lengths shown in table 3.

A complementary view can be found by considering the component and total energy spectra. Fluid–fluid spectra were obtained directly from the spectral representation of the fluid phase, whereas the particle–fluid and particle–particle spectra were determined by transforming the physical space correlations. As noted in §6, computing the Fourier transform of the correlations required the use of windowing functions (Sundaram 1996) to eliminate the high-frequency noise generated by the transform process. Some confidence was gained by comparing the fluid–fluid spectrum determined from the correlation with one obtained directly in Fourier space. In general, we observe that windowing functions have little effect on the low to

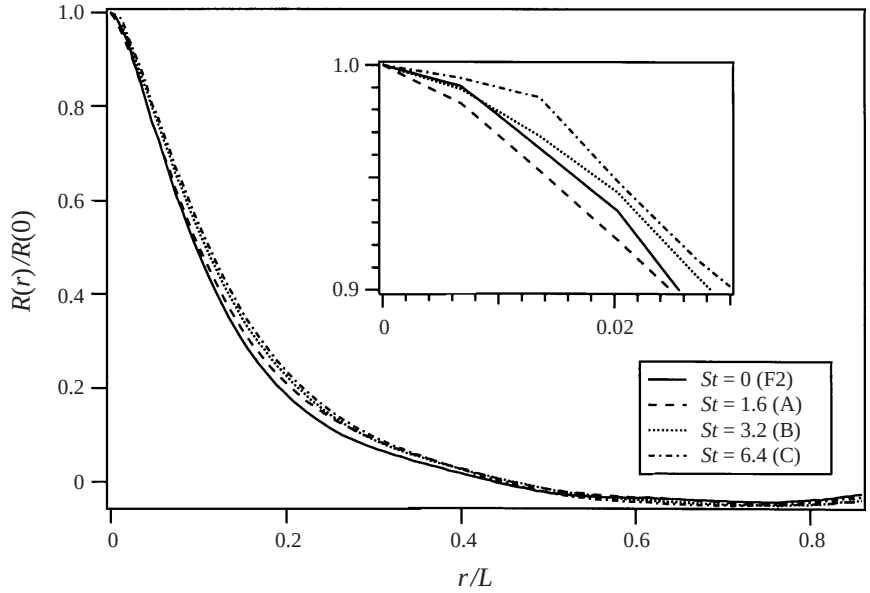

FIGURE 10. Total (fluid+particle) energy correlation as a function of the separation distance, r ($r > \sigma$) at three values of the Stokes number and the F2 run. The insert is a blowup of the small-r behaviour.

moderate wavenumber range, but can systematically influence the high wavenumber part of the spectrum. Thus, some caution is required in interpreting the trends in spectra beyond a wavenumber of approximately 32. The three component spectra for run B are summarized in figure 11. The insert shows a magnified view of the low wavenumber behaviour. Notice that the fluid–fluid spectrum is the weakest of the three at small wavenumbers, but is dominant at intermediate to high wavenumbers. This again indicates that the dominant scale for the fluid–fluid correlation lies at a higher wavenumber (smaller scale) than the dominant scales for the particle–fluid or particle–particle correlations. It is also interesting to note that the fluid–fluid spectrum is greatly enhanced at high wavenumbers due to the source from the particles. This has been referred to in the literature as the spectral *pivot* (Squires & Eaton 1990; Elghobashi & Truesdell 1993). This pivot enhances the rate of dissipation of energy in the fluid and is therefore consistent with the arguments presented in §5. We will discuss the pivot of the fluid energy spectrum in greater detail shortly.

Technically, the integral of the particle–fluid spectrum over all k must vanish to satisfy a kinematic constraint. It is therefore anticipated that the particle–fluid spectrum must change sign at high wavenumbers so as to satisfy the integral constraint. A careful analysis of the spectrum at high wavenumbers indeed shows that the spectrum changes sign at $k > 1/\sigma$. This negative region is not seen in figure 11 because of the limited range of k that is shown.

The normalized spectra for the Stokes number study (Runs A, B, C, and F2) are shown in figure 12. Notice that the total energy spectra (figure 12*a*) show a pivot with Stokes number at low wavenumbers. That is, the fraction of energy at the lowest wavenumbers increases with the particle Stokes number, whereas the reverse is true at intermediate wavenumbers. A similar trend is also observed in the component spectra (see figure 12*b–d*); once again, the particle–particle spectrum shows the strongest trend,

Run	F–F	F–P	P–P
F1	0.8074	—	—
F2	0.7843	—	—
A	0.8481	0.8949	0.9117
B	0.8683	0.9675	1.0253
C	0.8728	1.0807	1.1888
D	0.8839	0.9884	1.0459
F	0.8575	0.9721	0.9920
G	0.8292	0.9493	1.0150

TABLE 3. Integral lengths calculated for all three types of correlations from all runs at $T = 3.77$, where F denotes fluid and P particle. Particle velocities are observed to correlate the strongest with fluid correlating the least. Also note that the lengths increase with both inertia and loading (albeit much more weakly).

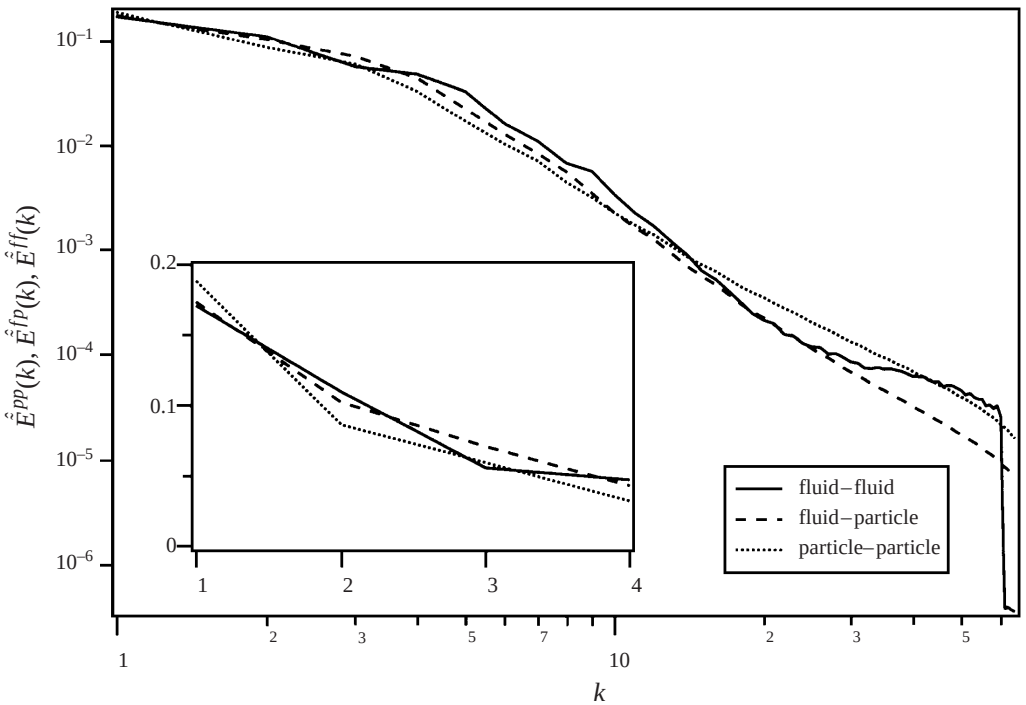

FIGURE 11. Comparison of the three component spectra from run B ($k < 1/\sigma$). The fluid–fluid spectrum was obtained directly from the Fourier transform of the fluid velocity, while the others were obtained by transforming the correlations. Fluid–fluid energies are in general larger than the fluid–particle or particle–particle spectra except at the lowest wavenumbers. The insert is a blowup of the small-k behaviour.

followed by the fluid–particle and fluid–fluid spectra. This low-wavenumber pivot is the spectral manifestation of the increase in the correlation length described earlier.

The fluid–fluid spectra shown in figure 12(b) are unique in that they also exhibit a pivot at high wavenumbers, as noted in earlier investigations (Squires & Eaton 1990; Elghobashi & Truesdell 1993). Particles absorb energy from the large-scale sweeping motions of the fluid and, via disturbance flows, liberate energy at small scales. The net

effect is a decrease in the total energy content of the fluid and an increase in the rate of dissipation of energy in the fluid. Consistent with earlier investigations, the degree of pivoting in the spectrum increases with increasing particle Stokes number. However, contrary to earlier reports (Elghobashi & Truesdell 1993), the crossover point appears to vary with Stokes number and time. In an effort to reconcile this variation, the fluid–fluid energy spectra are re-plotted in figure 13 against wavenumbers that are scaled by the Taylor microscale ($k\lambda(t)/4\pi$). As can be seen, the crossover wavenumbers substantially collapse in this modified coordinate system (over 70% reduction in the spread in the crossover wavenumber). The suggestion of scaling the pivot point with the Taylor microscale seems reasonable. On account of the direct transfer of energy by particles from large scales ($O(l_e)$) to scales on the order of the particle size ($\sigma < \eta$), one expects some intermediate scaling between the two to define the pivot. Assuming the universality of the Kolmogorov spectrum, the pivot would not be expected to occur in the one-parameter inertial range where the spectrum is determined wholly by the dissipation rate, ϵ. Instead, one would expect the pivot wavenumber to lie beyond the inertial and in the initial portion of the dissipation region, where $E(k)$ is determined by a combination of the dissipation rate and the kinematic viscosity, ν, i.e. where the Taylor microscale is located.

7.1. *A view of turbulence modulation by particles*

The presence of two pivots in the total energy spectrum (at low and high wavenumbers) suggests an explanation for the suppression and enhancement of turbulence that can occur with the introduction of particles to a turbulent flow field. The shift of energy to high wavenumbers in the fluid phase will clearly increase the viscous dissipation rate, as has already been shown. On the other hand, the pivot at low wavenumbers, in the presence of a mean shear (as would be found in an inhomogeneous flow), may increase the rate of production of turbulent energy as well. This can be seen, for example, by considering the source term in the standard k–ϵ equation. This term is usually modelled as a turbulent viscosity multiplied by the mean velocity gradient squared. As the turbulent viscosity is proportional to the integral scale of the turbulence, the increase in the integral scale caused by the particles could lead to a higher rate of production of turbulent energy. Thus, depending on the circumstances (i.e. the particle Stokes number and loading) it is plausible that the presence of particles may lead to an augmentation of turbulence, if the increase in production outweighs the enhanced dissipation rate, and suppression of turbulence if the reverse is true. Furthermore, since production and dissipation are usually large numbers with a small difference, the result of a small bias one way or the other can ultimately lead to a significant change in the turbulent kinetic energy. It must be emphasized that since the present simulations contain no source terms, the suggested mechanism is only speculation. Nevertheless, in the light of the continuing controversy regarding the role of particles in turbulent flows, the result may explain some of the conflicting explanations for this phenomenon in the literature.

8. Summary

Direct numerical simulations of a volumetrically dilute, yet appreciably mass loaded, suspension of finite-sized particles in a homogeneous turbulent fluid were performed on a 128^3 fluid grid using up to 64^3 particles. Particle diameters were kept sufficiently small so as to ensure that the local Reynolds number characterizing the flow around each particle remained small, enabling the use of Stokes drag to describe the force

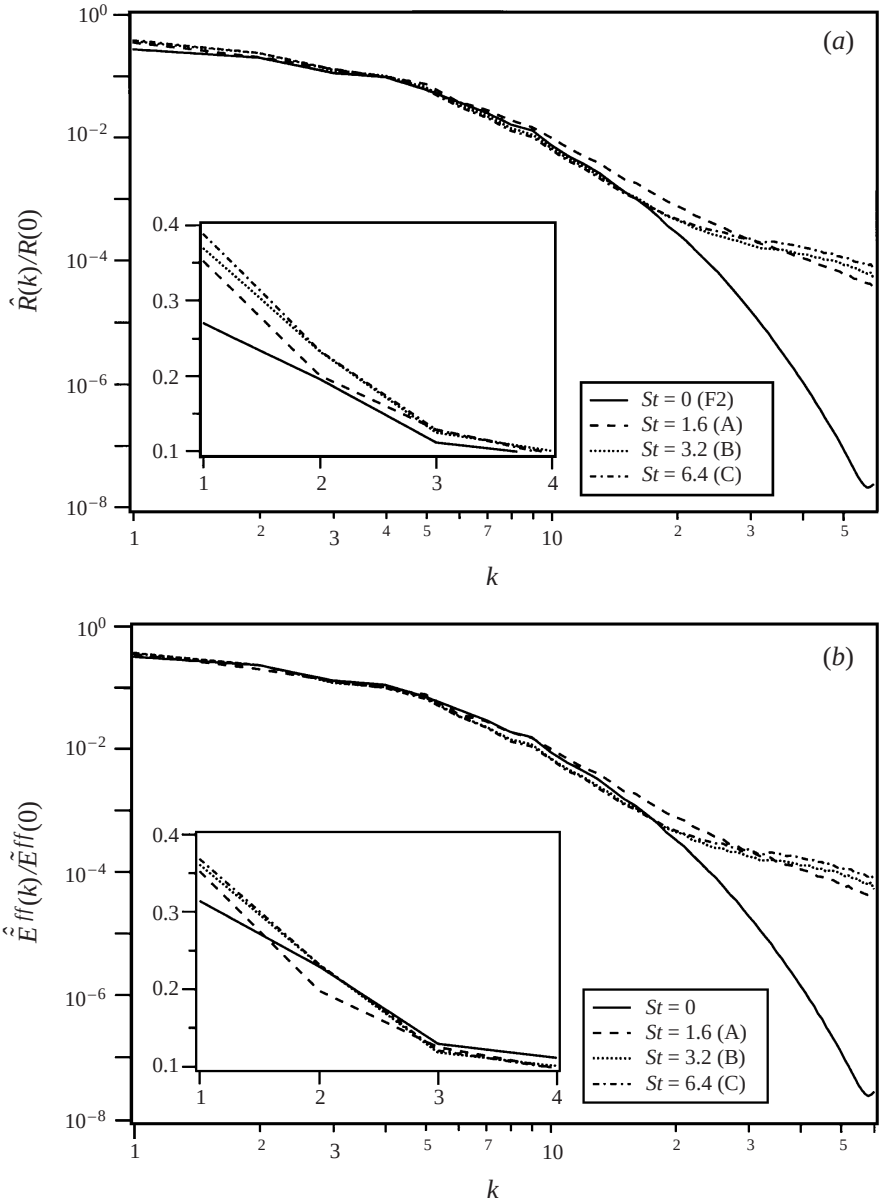

FIGURE 12 (a, b). For caption see facing page.

on the particle. In addition, particle collisions were treated as elastic or momemtum and energy conserving. These assumptions provide the absolute simplest (non-trivial) system to examine turbulence modulation. The emphasis of this investigation was on understanding the spectral dynamics of the energy associated with the fluid and particle phases. A novel two-field formalism that treats the particle and fluid phases as a single 'pseudo-fluid' has been extended to compute two-point energy correlations and spectra of the particle-laden flow field. The methodology outlined in this paper is a natural way of extending spectral analysis to particulate flows in a manner such that all single-point limits and other constraints are explicitly obeyed. The formalism

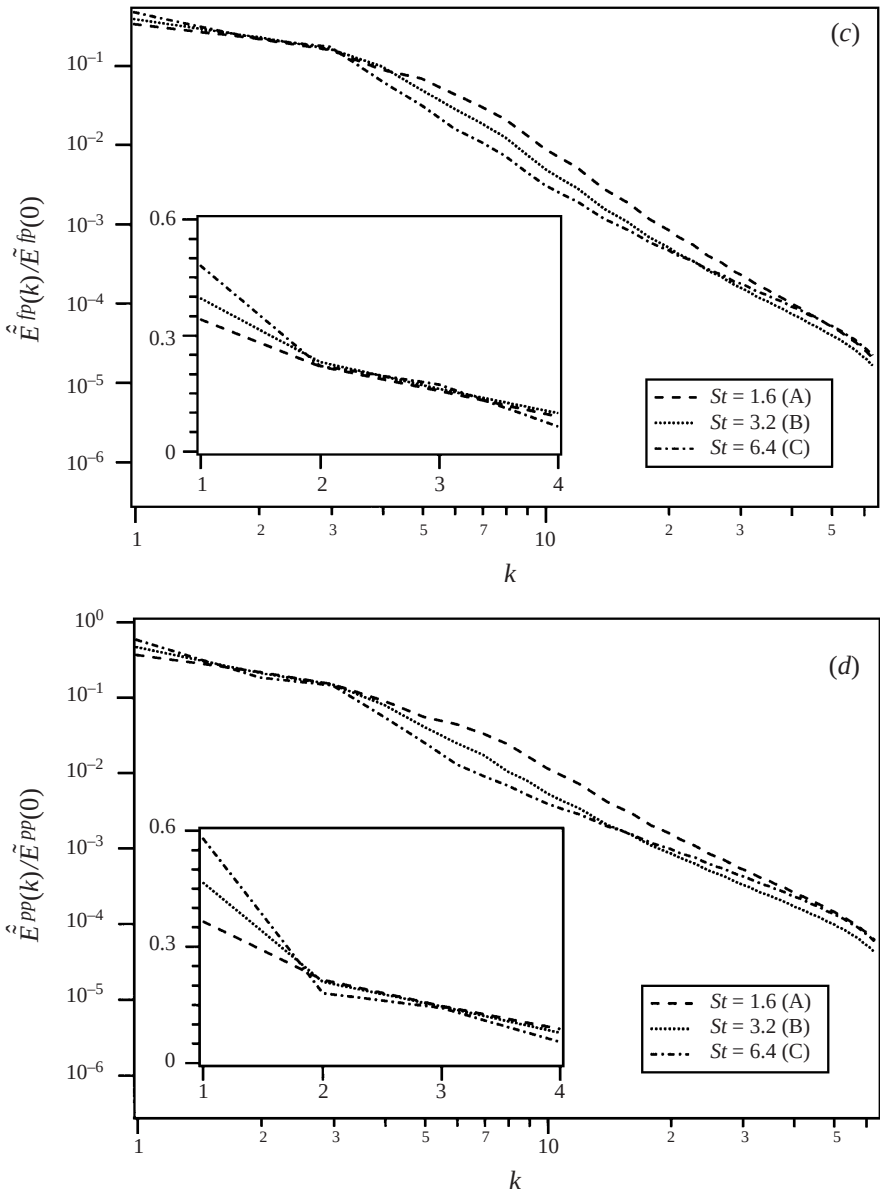

FIGURE 12. (*a*) Total (*b*) fluid–fluid (*c*) fluid–particle (*d*) particle–particle spectra are shown in order ($k < 1/\sigma$). All spectra display a crossover at small k (see inserts). Fluid–fluid and the total energy spectra show the more classical pivot at larger k associated with particle feedback. Contrary to prior investigations, this second crossover wavenumber is observed to vary with particle inertia.

decomposes the total energy spectrum into separate contributions involving specific particle–particle, particle–fluid, and fluid–fluid correlations. Unknown correlations required by the theory were then determined from the direct numerical simulation databases. The notion of separating correlations and spectra into distinct particle, fluid and inter-phase correlations was shown to be not only viable but also extremely valuable in analysing the behaviour of particulate turbulent flows. By studying the response of the spectra to changes in the parameter values, new insights into the mechanisms responsible for turbulence modulation by particles were obtained.

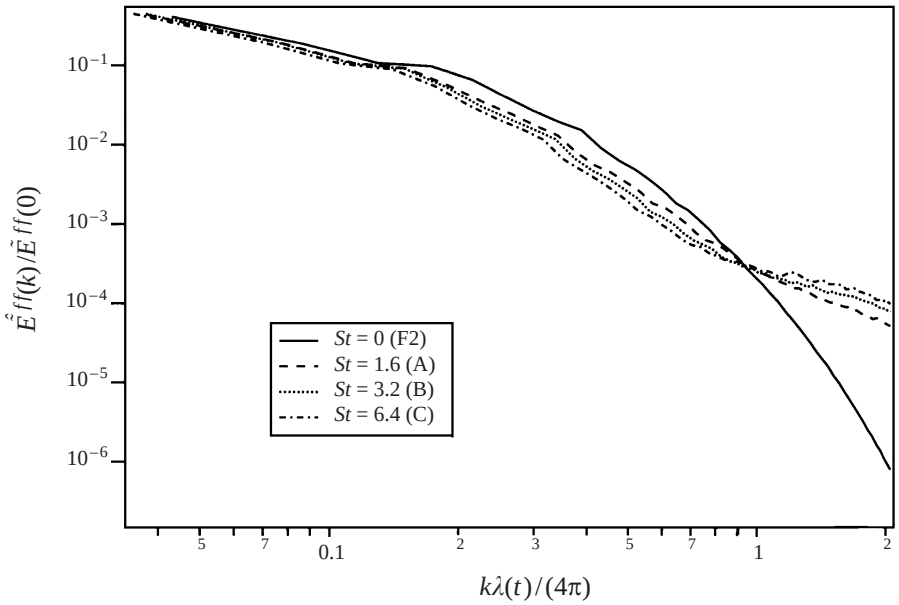

FIGURE 13. Fluid energy spectra, at $T = 1.89$ are plotted against wavenumbers scaled by the Taylor microscale. The variation in the crossover wavenumber was reduced by over 70%.

The key non-dimensional parameters for a monodisperse system of particles are the Stokes number, the volume fraction of particles and the mass fraction of particles. In one parametric study, the particle Stokes number was systematically varied while holding the volumetric and mass loadings constant. A second, complementary study was also performed in which the particle Stokes number was fixed while the volumetric and mass loadings were varied simultaneously by changing the total number of particles. The simplest physical arguments suggest that in the dilute limit, particles should act independently, and so all extrinsic effects of the particles should scale linearly with the total number of particles. Indeed, this was confirmed by the loading study. Both the magnitude of the particle dissipation (Φ_p) and the enhancement in the viscous dissipation ($\Delta\Phi_v$) were found to scale nearly linearly with the particle number density.

Single-point turbulent kinetic energies (fluid + particle) determined from the simulations were observed to decrease monotonically with increasing particle Stokes number and/or load. The apparent cause can be traced to two effects: (i) the rate of viscous dissipation of turbulent energy was enhanced by particles; and (ii) the particles introduced a second particle drag dissipation mechanism. The first effect is related to the well known pivot in the fluid energy spectrum caused by the particles.

The two-point density correlation (spectrum) was shown to be completely characterized by two functions: (i) the Overlap function; and (ii) the particle–particle radial distribution function (RDF). The Overlap function is a geometric function that depends on the shape of the particles only (spheres in this case), whereas the RDF describes the spatial distribution of the particles. The contribution to the density correlation (spectrum) from the Overlap function was shown to dominate that from the RDF at large k. Nevertheless, it is the RDF (and the spatial information therein) that ultimately controls the dynamics of the two-phase system. It is important to note that a single-point description of a particle-laden system cannot distinguish these vastly different contributions to the density correlation, whereas the distinction arises naturally in a two-point formulation.

At the particle loadings considered in this study, the RDF for a uniformly distributed particle field would nearly equal unity for all separation distances larger than the particle diameter. However, owing to a phenomenon known as preferential concentration, the RDFs from the simulations were substantially greater than unity. The degree of preferential concentration was found to be sensitive to the particle Stokes number, but was only weakly dependent on the particle loading. Equivalent trends were observed in the Fourier transforms of the RDFs as well. For example, the first peak in the spectrum shifted towards higher wavenumbers as the particle Stokes number decreased, indicating that interparticle separation distances were shrinking (or the system was becoming more strongly concentrated).

Next, two-point component and total energy correlations and spectra were determined from the DNS data. At small separations, the particle–particle correlations decayed more quickly than either the fluid–particle or fluid–fluid ones. Similarly in Fourier space, the particle–particle spectrum was observed to pivot at low wavenumbers causing an increase in the integral scale of the system. The explanation appears to be related to the greater inertia of the particles. Particles that are strongly correlated at one instant tend not to decorrelate as rapidly as fluid points, owing to their greater inertia; consequently their correlation length is greater than that for equivalent fluid elements.

This lends evidence to an alternative explanation for the mechanism by which particles sometimes enhance and other times diminish turbulence. We have shown that particles, in the absence of source terms, can only increase the rate of dissipation. However, if a source term were also present (due to mean shear, for example), the presence of particles may increase the integral length scale of the turbulence and thereby increase the production rate as well. This suggests that in a particle-laden flow with mean shear, a competition arises between the enhancement in the production and dissipation rates. That competition is parameterized by the particle Stokes number and loading. As production and dissipation are often two large numbers whose difference is small, even a small bias one way or the other can have a profound effect on the turbulent kinetic energy. Future studies will focus on the energy production mechanism in a homogeneous turbulent shear flow (for instance) to test the proposed hypothesis.

All computations were performed on the CRAY YMP-C90 at the Pittsburgh Supercomputing Center under grant CTS930052P. The authors also acknowledge financial support for this study from Dow Chemical through the Young Minority Investigator Award (awarded to L.R.C.) and Arco Chemical.

Appendix A. Derivation of the two-field form of the generalized Reynolds stress

In this Appendix we derive the two-field form of the generalized Reynolds stress correlations (see (30)–(33)). The analysis is similar to the one used in Sundaram & Collins (1994*a*) for the density correlation. We begin by considering a volume V of fluid with a density ρ_f that contains N_p indistinguishable spherical particles embedded within, each of diameter σ, density ρ_p and response time τ_p. Let the particles, numbered $1, \cdots, N_p$, be characterized by their positions $\boldsymbol{x}^1, \cdots, \boldsymbol{x}^{N_p}$ and velocities $\boldsymbol{v}^1, \cdots, \boldsymbol{v}^{N_p}$. In general the particle and fluid densities are not matched, and so the suspension can be considered a variable-density 'pseudo-fluid' with discontinuous density changes at the particle interfaces. Under turbulent flow conditions, this pseudo-fluid will generate a Reynolds stress in much the same way that a pure fluid does. The Reynolds stress in a variable-density system can be defined in several different ways. Based on earlier

studies that favour density-weighted or Favre-averaged variables, we have selected the generalized Reynolds stress defined as

$$R_{ij}(\boldsymbol{x}, \boldsymbol{x}+\boldsymbol{r}) \equiv \overline{\rho(\boldsymbol{x}) u_i'(\boldsymbol{x}) u_j'(\boldsymbol{x}+\boldsymbol{r})}. \tag{A 1}$$

The particle density can be decomposed as follows:

$$\rho(\boldsymbol{x}) \equiv \beta_p(\boldsymbol{x})\rho_p + \beta_f(\boldsymbol{x})\rho_p. \tag{A 2}$$

Given the equivalent decomposition of the velocity field shown in (25), and further noting that $\beta_p^2(\boldsymbol{x}) = \beta_p(\boldsymbol{x})$; $\beta_f^2(\boldsymbol{x}) = \beta_f(\boldsymbol{x})$; and $\beta_p(\boldsymbol{x})\beta_f(\boldsymbol{x}) = 0$, the Reynolds stress in the pseudo-fluid can be decomposed into four terms (as shown in (27))

$$R_{ij}(\boldsymbol{r}) = R_{ij}^{pp}(\boldsymbol{r}) + R_{ij}^{ff}(\boldsymbol{r}) + R_{ij}^{fp}(\boldsymbol{r}) + R_{ij}^{pf}(\boldsymbol{r}). \tag{A 3}$$

In principle, the above correlations can be evaluated from the DNS; however the expressions contain particle-phase-averaged properties that would be difficult to determine directly from the simulations. By taking advantage of the fact that the density and velocity everywhere within a given particle is constant, it is possible to express these relationships in terms of particle centre statistics (i.e. the radial distribution functions and velocity correlations), thereby eliminating the need to average over the particle phase. The derivation for each component correlation is given in the subsections below.

A.1. *Two-field representation for* $R_{ij}^{pp}(\boldsymbol{r})$

The particle-particle component of the Reynolds stress is defined as

$$R_{ij}^{pp}(\boldsymbol{r}) = \rho_p \, \overline{\beta_p(\boldsymbol{x}) v_i(\boldsymbol{x}) \, \beta_p(\boldsymbol{x}+\boldsymbol{r}) v_j(\boldsymbol{x}+\boldsymbol{r})}. \tag{A 4}$$

Substituting the relationships for $\beta_p(\boldsymbol{x})$ from (3) yields

$$R_{ij}^{pp}(\boldsymbol{r}) = \rho_p \quad \overline{\sum_{m=1}^{N_p} H\left(\tfrac{1}{2}\sigma - |\boldsymbol{x} - \boldsymbol{x}^m|\right) v_i^m \sum_{n=1}^{N_p} H\left(\tfrac{1}{2}\sigma - |\boldsymbol{x} + \boldsymbol{r} - \boldsymbol{x}^n|\right) v_j^n} \tag{A 5}$$

Since the particles are indistinguishable, the above relationship can be divided into two terms. The first term is the intra-particle correlations resulting from two points lying within a single particle (obviously, the separation distance between the two points, r, must be smaller than σ). The second term results from inter-particle correlations resulting from points lying within two different particles. The result of this separation is

$$\begin{aligned} R_{ij}^{pp}(\boldsymbol{r}) = & \underbrace{\rho_p N_p \quad \overline{H\left(\tfrac{1}{2}\sigma - |\boldsymbol{x} - \boldsymbol{x}^1|\right) v_i^1 \, H\left(\tfrac{1}{2}\sigma - |\boldsymbol{x} + \boldsymbol{r} - \boldsymbol{x}^1|\right) v_j^1}}_{\text{single-particle}} \\ & + \underbrace{\rho_p N_p (N_p - 1) \overline{H\left(\tfrac{1}{2}\sigma - |\boldsymbol{x} - \boldsymbol{x}^1|\right) v_i^1 \, H\left(\tfrac{1}{2}\sigma - |\boldsymbol{x} + \boldsymbol{r} - \boldsymbol{x}^2|\right) v_j^2}}_{\text{two-particle}}. \end{aligned} \tag{A 6}$$

For an isotropic flow field the single-particle term is given by

$$\begin{aligned} \text{single-particle} &= \rho_p \underbrace{N_p H\left(\tfrac{1}{2}\sigma - |\boldsymbol{x} - \boldsymbol{x}^1|\right) H\left(\tfrac{1}{2}\sigma - |\boldsymbol{x} + \boldsymbol{r} - \boldsymbol{x}^1|\right)}_{\alpha_p I(r)/V_p} \overline{v_i^1 v_j^1} \\ &= \rho_p \frac{\alpha_p}{V_p} I(r) \frac{\overline{v^2}}{3} \delta_{ij}, \end{aligned} \tag{A 7}$$

where δ_{ij} is the Kronecker delta function.

The two-particle term requires a few steps before it can be reduced to an equivalent form. First, we can re-express the Heaviside functions as

$$H\left(\tfrac{1}{2}\sigma - |\boldsymbol{x}-\boldsymbol{x}^1|\right) = \int_V H\left(\tfrac{1}{2}\sigma - |\boldsymbol{x}-\boldsymbol{R}_1|\right)\delta(\boldsymbol{R}_1-\boldsymbol{x}^1)\mathrm{d}\boldsymbol{R}_1. \tag{A 8}$$

Substituting into the two-particle term in (A 6) yields

$$\begin{aligned}\text{two-particle} = \rho_p \int_V\int_V \mathrm{d}\boldsymbol{R}_1\mathrm{d}\boldsymbol{R}_2 H\left(\tfrac{1}{2}\sigma - |\boldsymbol{x}-\boldsymbol{R}_1|\right) H\left(\tfrac{1}{2}\sigma - |\boldsymbol{x}+\boldsymbol{r}-\boldsymbol{R}_2|\right)\\ \times N_p(N_p-1)\overline{\delta(\boldsymbol{R}_1-\boldsymbol{x}^1)\delta(\boldsymbol{R}_2-\boldsymbol{x}^2)v_i^1 v_j^2}.\end{aligned} \tag{A 9}$$

Then making the substitution $\boldsymbol{z} \equiv \boldsymbol{R}_2 - \boldsymbol{R}_1$, we obtain

$$\begin{aligned}\text{two-particle} = \rho_p N_p(N_p-1)\int_V d\boldsymbol{z}\,\overline{\delta(\boldsymbol{R}_1-\boldsymbol{x}^1)\delta(\boldsymbol{z}+\boldsymbol{R}_1-\boldsymbol{x}^2)v_i^1 v_j^2}\\ \times \underbrace{\int_V H\left(\tfrac{1}{2}\sigma - |\boldsymbol{x}-\boldsymbol{R}_1|\right) H\left(\tfrac{1}{2}\sigma - |\boldsymbol{x}+\boldsymbol{r}-\boldsymbol{z}-\boldsymbol{R}_1|\right)\mathrm{d}\boldsymbol{R}_1}_{I(|\boldsymbol{r}-\boldsymbol{z}|)}.\end{aligned} \tag{A 10}$$

Analogous to procedures in statistical mechanics (McQuarrie 1976) the above relationship can be re-expressed in terms of a conditional average and a radial distribution function defined as

$$\frac{\alpha_p^2}{V_p^2}\tilde{g}^{pp}(\boldsymbol{z}) \equiv N_p(N_p-1)\overline{\delta(\boldsymbol{x}-\boldsymbol{x}^1)\,\delta(\boldsymbol{x}+\boldsymbol{r}-\boldsymbol{x}^2)}. \tag{A 11}$$

Using the above function

$$\text{two-particle} = \rho_p \int_V \frac{\alpha_p^2}{V_p^2} I(|\boldsymbol{r}-\boldsymbol{z}|)\tilde{g}^{pp}(\boldsymbol{z})\left[\overline{v_i^1 v_j^2 \mid \boldsymbol{x}^1 = \boldsymbol{R}_1, \boldsymbol{x}^2 = \boldsymbol{R}_1+\boldsymbol{z}}\right]\mathrm{d}\boldsymbol{z}. \tag{A 12}$$

The conditional average has been defined as $\tilde{E}_{ij}^{pp}(\boldsymbol{z})$. Substituting this definition above yields

$$\text{two-particle} = \rho_p \frac{\alpha_p^2}{V_p^2}\int_V \tilde{g}^{pp}(\boldsymbol{z}) I(|\boldsymbol{r}-\boldsymbol{z}|)\tilde{E}_{ij}^{pp}(\boldsymbol{z})\mathrm{d}\boldsymbol{z}. \tag{A 13}$$

Collecting both the single- and two-particle terms and substituting into (A 6) yields the final relationship shown in the text (see (33))

$$R_{ij}^{pp}(\boldsymbol{r}) = \rho_p \frac{\overline{v^2}}{3}\frac{\alpha_p}{V_p} I(|\boldsymbol{r}|)\delta_{ij} + \left(\frac{\alpha_p}{V_p}\right)^2 \rho_p \int_V \tilde{g}^{pp}(|\boldsymbol{z}|)\tilde{E}_{ij}^{pp}(|\boldsymbol{z}|) I(|\boldsymbol{r}-\boldsymbol{z}|)\,\mathrm{d}\boldsymbol{z}. \tag{A 14}$$

A.2. *Two-field representation for* $R_{ij}^{fp}(\boldsymbol{r})$ *or* $R_{ij}^{pf}(\boldsymbol{r})$

The methodology to decompose $R_{ij}^{fp}(\boldsymbol{r})$ and $R_{ij}^{pf}(\boldsymbol{r})$ is essentially the same, so to illustrate the approach we will only consider the former. The fluid-particle component of the Reynolds stress correlation is defined as

$$R_{ij}^{fp}(\boldsymbol{r}) = \rho_f\,\overline{\beta_f(\boldsymbol{x})u_i(\boldsymbol{x})\,\beta_p(\boldsymbol{x}+\boldsymbol{r})v_j(\boldsymbol{x}+\boldsymbol{r})}. \tag{A 15}$$

Substituting the relationships for $\beta_p(\boldsymbol{x})$ from (3) yields

$$R_{ij}^{fp}(\boldsymbol{r}) = \rho_f \; \overline{\beta_f(\boldsymbol{x}) u_i(\boldsymbol{x}) \sum_{n=1}^{N_p} H\left(\tfrac{1}{2}\sigma - |\boldsymbol{x}+\boldsymbol{r}-\boldsymbol{x}^n|\right) v_j^n}. \tag{A 16}$$

Once again, the relationship can be simplified by recognizing that the particles are indistinguishable and so the sum over N_p particles can be replaced by

$$R_{ij}^{fp}(\boldsymbol{r}) = \rho_f \; N_p \; \overline{\beta_f(\boldsymbol{x}) u_i(\boldsymbol{x}) H\left(\tfrac{1}{2}\sigma - |\boldsymbol{x}+\boldsymbol{r}-\boldsymbol{x}^1|\right) v_j^1}. \tag{A 17}$$

Taking advantage of (A 8) we obtain

$$R_{ij}^{fp}(\boldsymbol{r}) = \rho_f \; N_p \int_V d\boldsymbol{R}_1 H\left(\tfrac{1}{2}\sigma - |\boldsymbol{x}+\boldsymbol{r}-\boldsymbol{R}_1|\right) \overline{\beta_f(\boldsymbol{x}) u_i(\boldsymbol{x}) \delta(\boldsymbol{x}^1 - \boldsymbol{R}_1) v_j^1}. \tag{A 18}$$

If we define $\tilde{g}^{fp}(\boldsymbol{r})$ as

$$\tilde{g}^{fp}(\boldsymbol{r}) \equiv \frac{N_p V_p}{\alpha_p \alpha_f} \; \overline{\beta_f(\boldsymbol{x}) \delta(\boldsymbol{x}+\boldsymbol{r}-\boldsymbol{x}^1)} \tag{A 19}$$

(note that the normalization of $\tilde{g}^{fp}(\boldsymbol{r})$ is chosen such that it reduces to unity for a uniform particle concentration) the correlation shown in (A 18) can be re-expressed in terms of a conditional average

$$R_{ij}^{fp}(\boldsymbol{r}) = \rho_f \left(\frac{\alpha_p \alpha_f}{V_p}\right) \int_V H\left(\tfrac{1}{2}\sigma - |\boldsymbol{x}+\boldsymbol{r}-\boldsymbol{R}_1|\right) \tilde{g}^{fp}(|\boldsymbol{R}_1 - \boldsymbol{x}|) \times \left[\overline{u_i(\boldsymbol{x}) v_j^1 \mid \beta_f(\boldsymbol{x}) = 1; \boldsymbol{x}^1 = \boldsymbol{R}_1}\right]. \tag{A 20}$$

The conditional average has been defined as $\tilde{E}_{ij}^{fp}(\boldsymbol{z})$. Substituting this above and letting $\boldsymbol{z} \equiv \boldsymbol{R}_1 - \boldsymbol{x}$ we obtain (see (31))

$$R_{ij}^{fp}(\boldsymbol{r}) = \rho_f \left(\frac{\alpha_p \alpha_f}{V_p}\right) \int_V H\left(\tfrac{1}{2}\sigma - |\boldsymbol{r}-\boldsymbol{z}|\right) \tilde{g}^{fp}(|\boldsymbol{z}|) \tilde{E}_{ij}^{fp}(\boldsymbol{z}) \, \mathrm{d}\boldsymbol{z}. \tag{A 21}$$

A.3. *Two-field representation for* $R_{ij}^{ff}(\boldsymbol{r})$

As the fluid-fluid correlation does not involve the particle phase, there is no need to eliminate the particle-phase averaging as in the previous examples. Hence, the only real modification that is made here is to replace the fluid-fluid correlation by a conditionally averaged velocity correlation multiplied by an appropriate RDF (as was done in the previous examples). We begin with the definition of the correlation

$$R_{ij}^{ff}(\boldsymbol{r}) = \rho_f \; \overline{\beta_f(\boldsymbol{x}) u_i(\boldsymbol{x}) \; \beta_f(\boldsymbol{x}+\boldsymbol{r}) u_j(\boldsymbol{x}+\boldsymbol{r})}. \tag{A 22}$$

If we define the fluid-fluid RDF as

$$\tilde{g}^{ff}(\boldsymbol{r}) \equiv \frac{1}{\alpha_f^2} \; \overline{\beta_f(\boldsymbol{x}) \beta_f(\boldsymbol{x}+\boldsymbol{r})} \tag{A 23}$$

then the Reynolds stress can be re-expressed as

$$R_{ij}^{ff}(\boldsymbol{r}) = \rho_f \alpha_f^2 \tilde{g}^{ff}(\boldsymbol{r}) \quad \left[\overline{u_i(\boldsymbol{x}) u_j(\boldsymbol{x}+\boldsymbol{r}) \mid \beta_f(\boldsymbol{x}) = 1; \beta_f(\boldsymbol{x}+\boldsymbol{r}) = 1}\right]. \tag{A 24}$$

The conditional average in the above equation was defined as $\tilde{E}_{ij}^{ff}(\boldsymbol{z})$. Substituting yields the final relationship (see (30))

$$R_{ij}^{ff}(\boldsymbol{r}) = \rho_f \alpha_f^2 \tilde{g}^{ff}(\boldsymbol{r}) \tilde{E}_{ij}^{ff}(\boldsymbol{r}). \tag{A 25}$$

Appendix B. Generalized expressions for density and Reynolds stress correlations and spectra

The complete and rigorous expressions for the two-point density and Reynolds stress correlations at arbitrary loadings and with homogeneous, but not necessarily isotropic, turbulence are summarized in this Appendix for completeness.

B.1. *Physical space*

$$B(\boldsymbol{r}) = \left[\frac{\alpha_p}{V_p} I(|\boldsymbol{r}|) + \left(\frac{\alpha_p}{V_p}\right)^2 \int_V \tilde{h}^{pp}(|\boldsymbol{z}|) I(|\boldsymbol{r}-\boldsymbol{z}|)\, \mathrm{d}\boldsymbol{z}\right] (\rho_p - \rho_f)^2, \tag{B 1}$$

$$R_{ij}^{ff}(\boldsymbol{r}) = \alpha_f^2 \rho_f \tilde{g}^{ff}(\boldsymbol{r}) \tilde{E}_{ij}^{ff}(\boldsymbol{r}), \tag{B 2}$$

$$R_{ij}^{fp}(\boldsymbol{r}) = \left(\frac{\alpha_p \alpha_f}{V_p}\right) \rho_f \int_V H\left(\tfrac{1}{2}\sigma - |\boldsymbol{r}-\boldsymbol{z}|\right) \tilde{g}^{fp}(\boldsymbol{z}) \tilde{E}_{ij}^{fp}(\boldsymbol{z})\, \mathrm{d}\boldsymbol{z}, \tag{B 3}$$

$$R_{ij}^{pf}(\boldsymbol{r}) = \left(\frac{\alpha_p \alpha_f}{V_p}\right) \rho_p \int_V H\left(\tfrac{1}{2}\sigma - |\boldsymbol{r}-\boldsymbol{z}|\right) \tilde{g}^{pf}(\boldsymbol{z}) \tilde{E}_{ij}^{pf}(\boldsymbol{z})\, \mathrm{d}\boldsymbol{z}, \tag{B 4}$$

$$R_{ij}^{pp}(\boldsymbol{r}) = \rho_p \frac{\overline{v_p^2}}{3} \frac{\alpha_p}{V_p} I(|\boldsymbol{r}|)\delta_{ij} + \left(\frac{\alpha_p}{V_p}\right)^2 \rho_p \int_V \tilde{g}^{pp}(|\boldsymbol{z}|) \tilde{E}_{ij}^{pp}(|\boldsymbol{z}|) I(|\boldsymbol{r}-\boldsymbol{z}|)\, \mathrm{d}\boldsymbol{z}, \tag{B 5}$$

where

$$\tilde{g}^{ff}(\boldsymbol{r}) = 1 + \frac{1}{\alpha_f^2}\left[\frac{\alpha_p}{V_p} I(|\boldsymbol{r}|) + \left(\frac{\alpha_p}{V_p}\right)^2 \int_V I(|\boldsymbol{r}-\boldsymbol{z}|) \tilde{h}^{pp}(\boldsymbol{z})\, \mathrm{d}\boldsymbol{z}\right], \tag{B 6}$$

$$\tilde{g}^{fp}(\boldsymbol{r}) = 1 - \frac{1}{\alpha_f} H\left(\tfrac{1}{2}\sigma - |\boldsymbol{r}|\right) - \frac{\alpha_p}{V_p \alpha_f} \int_V H\left(\tfrac{1}{2}\sigma - |\boldsymbol{r}-\boldsymbol{z}|\right) \tilde{h}^{pp}(\boldsymbol{z})\, \mathrm{d}\boldsymbol{z}, \tag{B 7}$$

$$\tilde{g}^{pf}(\boldsymbol{r}) = \tilde{g}^{fp}(-\boldsymbol{r}). \tag{B 8}$$

B.2. *Transform space*

$$\hat{B}(\boldsymbol{k}) = \frac{\alpha_p}{V_p} \hat{I}(|\boldsymbol{k}|) \left[1 + \frac{\alpha_p}{V_p} \hat{\tilde{h}}^{pp}(\boldsymbol{k})\right] (\rho_p - \rho_f)^2, \tag{B 9}$$

$$\hat{R}_{ij}(\boldsymbol{k}) = \hat{R}_{ij}^{ff}(\boldsymbol{k}) + \hat{R}_{ij}^{fp}(\boldsymbol{k}) + \hat{R}_{ij}^{pf}(\boldsymbol{k}) + \hat{R}_{ij}^{pp}(\boldsymbol{k}), \tag{B 10}$$

$$\hat{R}_{ij}^{ff}(\boldsymbol{k}) = \alpha_f^2 \rho_f\, \hat{\tilde{g}}^{ff}(\boldsymbol{k}) * \hat{\tilde{E}}_{ij}^{ff}(\boldsymbol{k}), \tag{B 11}$$

$$\hat{R}_{ij}^{fp}(\boldsymbol{k}) = \left(\frac{\alpha_p \alpha_f}{V_p}\right) \rho_f \hat{H}(|\boldsymbol{k}|)\, \hat{\tilde{g}}^{fp}(\boldsymbol{k}) * \hat{\tilde{E}}_{ij}^{fp}(\boldsymbol{k}), \tag{B 12}$$

$$\hat{R}_{ij}^{pf}(\boldsymbol{k}) = \left(\frac{\alpha_p \alpha_f}{V_p}\right) \rho_p \hat{H}(|\boldsymbol{k}|)\, \hat{\tilde{g}}^{pf}(\boldsymbol{k}) * \hat{\tilde{E}}_{ij}^{pf}(\boldsymbol{k}), \tag{B 13}$$

$$\hat{R}_{ij}^{pp}(\boldsymbol{k}) = \frac{\alpha_p \rho_p}{V_p} \hat{I}(|\boldsymbol{k}|) \left[\frac{\overline{v_p^2}}{3}\delta_{ij} + \frac{\alpha_p}{V_p} \hat{\tilde{g}}(\boldsymbol{k}) * \hat{\tilde{E}}_{ij}^{pp}(\boldsymbol{k})\right], \tag{B 14}$$

where

$$\hat{\tilde{g}}^{ff}(\boldsymbol{k}) = \delta(\boldsymbol{k}) + \frac{1}{\alpha_f^2} \frac{\alpha_p}{V_p} \hat{I}(\boldsymbol{k}) \left[1 + \frac{\alpha_p}{V_p} \hat{\tilde{h}}^{pp}(\boldsymbol{k})\right], \tag{B 15}$$

$$\hat{\tilde{g}}^{fp}(\boldsymbol{k}) = \delta(\boldsymbol{k}) - \frac{1}{\alpha_f}\hat{H}(\boldsymbol{k})\left[1 + \frac{\alpha_p}{V_p}\hat{\tilde{h}}^{pp}(\boldsymbol{k})\right], \tag{B 16}$$

and $*$ indicates a convolution and cf. $\hat{I}(|\boldsymbol{k}|)$ in (24). Also,

$$\hat{H}(|\boldsymbol{k}|) = 24V_p\frac{\left(\sin(k\sigma/2) - \frac{1}{2}k\sigma\cos(k\sigma/2)\right)}{(k\sigma)^3}. \tag{B 17}$$

REFERENCES

Besnard, D. C. & Harlow, F. H. 1985 Turbulence in two-field incompressible flow. *Tech. Rep.* LA-10187-MS. Los Alamos National Laboratory.

Besnard, D. C., Harlow, F. H. & Rauenzahn, R. 1987 Conservation and transport properties of turbulence with large density variations. *Tech. Rep.* LA-10911-MS. Los Alamos National Laboratory.

Besnard, D. C., Harlow, F. H., Rauenzahn, R. M. & Zemach, C. 1990 Spectral transport model for turbulence. *Tech. Rep.* LA-11821-MS. Los Alamos National Laboratory.

Canuto, C., Hussaini, M. Y., Quarteroni, A. & Zang, T. A. 1988 *Spectral Methods in Fluid Dynamics*. Springer.

Clark, T. T. & Spitz, P. M. 1994 A study of the two-point correlation equations for variable-density turbulence. *Tech. Rep.* LA-12671-MS. Los Alamos National Laboratory.

Crowe, C. T. 1982 Review-numerical models for dilute gas-particle flows. *Trans. ASME J. Fluids Engng* **104**, 297–303.

Crowe, C. T., Troutt, T. R. & Chung, J. N. 1996 Numerical models for two-phase turbulent flows. *Ann. Rev. Fluid Mech.* **28**, 11–43.

Elghobashi, S. 1991 Particle-laden turbulent flows: direct simulation and closure models. *Appl. Sci. Res.* **48**, 301–314.

Elghobashi, S. E. & Abou-Arab, T. W. 1983 A two-equation turbulence model for two-phase flows, *Phys. Fluids* A **26**, 931–938.

Elghobashi, S. E. & Truesdell, G. C. 1993 On the two-way interaction between homogeneous turbulence and dispersed particles. I: Turbulence modification. *Phys. Fluids* A **5**, 1790–1801.

Gore, R. & Crowe, C. T. 1989 Effects of particle size on modulating turbulence intensity. *Intl J. Multiphase Flow* **15**, 279–285.

Hetsroni, G. 1989 Particles-Turbulence interaction. *Intl J. Multiphase Flow* **15**, 735–746.

Hinze, J. O. 1975 *Turbulence*. McGraw-Hill.

Ishii, M. 1975 Thermo-Fluid Dynamic Theory of Two Phase Flow. Eyrolles.

Maxey, M. R. 1987 The gravitational settling of aerosol particles in homogeneous turbulence and random flow fields. *J. Fluid Mech.* **174**, 441–465.

Maxey, M. R. & Riley, J. J. 1983 Equation of motion for a small rigid sphere in a nonuniform flow. *Phys. Fluids* A **26**, 883–889.

McLaughlin, J. B. 1994 Numerical computation of particles-turbulence interaction. *Intl J. Multiphase Flow* **20**, 211–232.

Mcquarrie, D. A. 1976 Statistical Mechanics, Harper & Row.

Nitsche, J. M. & Batchelor, G. K. 1997 Break-up of a falling drop containing dispersed particles. *J. Fluid Mech.* **340**, 161–175.

Orszag, S. A. & Patterson, G. S. 1972 *Numerical Simulation of Turbulence*. Springer.

Pan, Y. & Banerjee, S. 1997 Numerical Investigation of the effects of large particles on wall-turbulence. *Phys. Fluids* **9**, 3786–3807.

Percus, J. K. & Yevick, G. J. 1958 Analysis of classical statistical mechanics by means of collective coordinates. *Phys. Rev.* **110**, 1–13.

Shirolkar, J. S., Coimbra, C. F. M. & McQuay, M. Q. 1996 Fundamental aspects of modeling turbuent particle dispersion in dilute flows. *Prog. Energy Combust. Sci.* **22**, 363–399.

Squires, K. D. & Eaton, J. K. 1990 Particle response and turbulence modification in isotropic turbulence. *Phys. Fluids* A **2**, 1191–1203.

Squires, K. D. & Eaton, J. K. 1991 Preferential concentration of particles by turbulence, *Phys. Fluids* A **3**, 1169–1178.

Sundaram, S. 1996 Direct numerical simulations and spectral analysis of turbulent flows laden with finite size particles. PhD thesis, The Pennsylvania State University.

Sundaram, S. & Collins, L. R. 1994*a* Spectrum of density fluctuations in a particle-fluid system - I. Monodisperse spheres. *Intl J. Multiphase Flow* **20**, 1021–1037.

Sundaram, S. & Collins, L. R. 1994*b* Spectrum of density fluctuations in a particle-fluid system - II. Polydisperse spheres. *Intl J. Multiphase Flow* **20**, 1039–1052.

Sundaram, S. & Collins, L. R. 1996 Numerical considerations in simulating a turbulent suspension of finite-volume particles. *J. Comput. Phys.* **124**, 337–350.

Sundaram, S. & Collins, L. R. 1997 Collision statistics in an isotropic, particle-laden turbulent suspension I. direct numerical simulations. *J. Fluid Mech.* **335**, 75–109.

Tsuji, Y. 1991 Review: Turbulence modification in fluid-solid flows. In *Gas-Solid Flows* (ed. D. E. Stock *et al.*) ASME-FED vol. 110, pp. 1–6

Wang, L. P. & Maxey, M. R. 1993 Settling velocity and concentration distribution of heavy particles in homogeneous isotropic turbulence. *J. Fluid Mech.* **256**, 27–68.

Yarin, L. P. & Hetsroni, G. 1994 Turbulence intensity in dilute two-phase flows – 3: The particles-turbulence interaction in dilute two-phase flow, *Intl J. Multiphase Flow* **20**, 27–44.

Yuan, Z. & Michaelides, E. E. 1994 Turbulence modulation in particulate flows – a theoretical approach. *Intl J. Multiphase Flow* **18**, 779–785.